# Ground and Space-Based Measurement of Rocket Engine Burns in the Ionosphere

P. A. Bernhardt, J. O. Ballenthin, J. L. Baumgardner, A. Bhatt, I. D. Boyd, J. M. Burt, R. G. Caton, A. Coster,
P. J. Erickson, J. D. Huba, G. D. Earle, C. R. Kaplan, J. C. Foster, K. M. Groves, R. A. Haaser, R. A. Heelis,
D. E. Hunton, D. L. Hysell, J. H. Klenzing, M. F. Larsen, F. D. Lind, T. R. Pedersen, R. F. Pfaff,
R. A. Stoneback, P. A. Roddy, S. P. Rodriquez, G. S. San Antonio, P. W. Schuck, C. L. Siefring,
C. A. Selcher, S. M. Smith, E. R. Talaat, J. F. Thomason, R. T. Tsunoda, and R. H. Varney

*Abstract*—On-orbit firings of both liquid and solid rocket motors provide localized disturbances to the plasma in the upper atmosphere. Large amounts of energy are deposited to ionosphere in the form of expanding exhaust vapors which change the composition and flow velocity. Charge exchange between the neutral exhaust molecules and the background ions (mainly $O^+$) yields energetic ion beams. The rapidly moving pickup ions excite plasma instabilities and yield optical emissions after dissociative recombination with ambient electrons. Line-of-sight techniques for remote measurements rocket burn effects include direct observation of plume optical emissions with ground and satellite cameras, and plume scatter with UHF and higher frequency radars. Long range detection with HF radars is possible if the burns occur in the dense part of the ionosphere. The exhaust vapors initiate plasma turbulence in the ionosphere that can scatter HF radar waves launched from ground transmitters. Solid rocket motors provide particulates that become charged in the ionosphere and may excite dusty plasma instabilities. Hypersonic exhaust flow impacting the ionospheric plasma launches a low-frequency, electromagnetic pulse that is detectable using satellites with electric field booms. If the exhaust cloud itself passes over a satellite, *in situ* detectors measure increased ion-acoustic wave turbulence, enhanced neutral and plasma densities, elevated ion temperatures, and magnetic field perturbations. All of these techniques can be used for long range observations of plumes in the ionosphere. To demonstrate such long range measurements, several experiments were conducted by the Naval Research Laboratory including the Charged Aerosol Release Experiment, the Shuttle Ionospheric Modification with Pulsed Localized Exhaust experiments, and the Shuttle Exhaust Ionospheric Turbulence Experiments.

*Index Terms*—Environmental factors, ionosphere, plasma measurements, plasma waves.

P. A. Bernhardt, J. D. Huba, and C. L. Siefring are with the Plasma Physics Division, Naval Research Laboratory, Washington, DC 20374 USA (e-mail: bern@ppd.nrl.navy.mil).

J. O. Ballenthin, R. G. Caton, K. M. Groves, D. E. Hunton, T. R. Pedersen, P. A. Roddy, and C. A. Selcher are with the Air Force Research Laboratory, Kirtland AFB, NM 87117 USA.

J. L. Baumgardner and S. M. Smith are with Center for Space Physics, Boston University, Boston, MA 02215 USA (e-mail: jeffreyb@bu.edu).

A. Bhatt, A. Coster, P. J. Erickson, J. C. Foster, and F. D. Lind are with the MIT Haystack Observatory, Westford, MA 01886-1299 USA (e-mail: abhatt@haystack.mit.edu; ajc@haystack.mit.edu).

I. D. Boyd and J. M. Burt are with University of Michigan, Ann Arbor, MI 48109 USA.

G. D. Earle, R. A. Haaser, R. A. Heelis, J. H. Klenzing, and R. A. Stoneback are with University of Texas at Dallas, Richardson, TX 75080-3021 USA.

C. R. Kaplan is with the Laboratory for Computational Physics and Fluid Dynamics, Naval Research Laboratory, Washington, DC 20374 USA.

D. L. Hysell and R. H. Varney are with Cornell University, Ithaca, NY 14853 USA.

M. F. Larsen is with the Department of Physics and Astronomy, Clemson University, Clemson, NC 29634 USA.

R. F. Pfaff and P. W. Schuck are with the Goddard Space Flight Center, Greenbelt, MD 20771 USA.

S. P. Rodriquez, G. S. San Antonio, and J. F. Thomason are with the Radar Division, Naval Research Laboratory, Washington, DC 20374 USA.

E. R. Talaat is with the Applied Physics Laboratory, Johns Hopkins University, Laurel, MD 20723 USA.

R. T. Tsunoda is with the SRI International, Menlo Park, CA 94025 USA.

Color versions of one or more of the figures in this paper are available online at http://ieeexplore.ieee.org.

Digital Object Identifier 10.1109/TPS.2012.2185814

## I. INTRODUCTION

ROCKET engine firings in a boost or a trajectory-altering phase often occur in the ionosphere. The ionospheric burns can provide several signatures for remote detection by a wide range of sensors. The high speed exhaust vapors can alter the electron density of the ionosphere providing large changes in the propagation of radar and radio signals. In addition, the ion composition can be changed resulting in the production of optical emissions by ion-molecule and ion-electron reactions. Finally, plasma waves are excited by the exhaust interactions in the ionosphere. The plume processes that occur in space plasmas are reviewed, and observations of these interactions are highlighted with examples from recent experiments.

The ionosphere is a spherical plasma layer that surrounds the earth (Fig. 1). The bulk of the ionosphere is contained in the F-region with peak densities between 200 and 400-km altitude. The primary ion in the F-region is O+. For singly charged species, the number of ions per unit volume is balanced by an equal number of electrons in the same unit volume. The peak plasma density of the F-layer can range from $10^3$ to $10^6$ cm$^{-3}$ depending on time of day, season, solar cycle, and geographic location. The F-Layer electron temperature is in the range of 500 to 3000 K corresponding to energies between 0.05 and 0.3 eV. The F-Layer $O^+$ ion temperature is between 500 and 2000 K. The ambient magnetic field strength is $B_0 \sim 28 \cdot 10^{-6}$ T. In the ionosphere, the plasma pressure is much less than the magnetic pressure as given by the formula $\beta \sim nkT/(B^2/2\mu 0) = 10^{-8}$. The transport properties of the plasma are determined by the number of ion collisions in one ion gyro orbit. In the F-region, both the ions and electrons are confined to
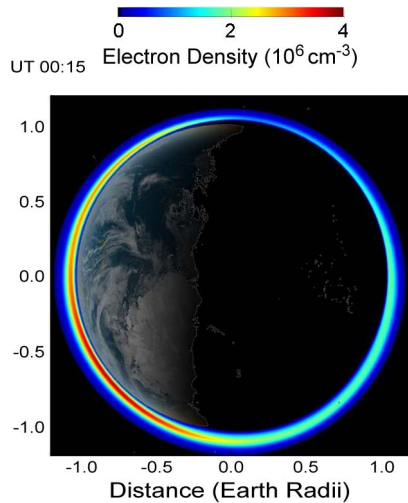
Fig. 1.   Model of the ionospheric layer around the earth provided by the NRL SAMI 3 model [1]. At sunrise (top of figure), the electron densities increase until about 2 PM (lower left) when maximum density is produced. After sunset, the F-layer decreases because the solar production of the plasma is cutoff by the absence of solar extreme ultraviolet rays.

magnetic field lines. The ions become unmagnetized at altitude below 100-km altitude where the ion gyro frequency $\Omega_i$ is less than the ion collision frequency $\nu_i$. All of these properties affect the ionospheric response to a rocket exhaust burn.

The basic theory of ionospheric modification is outlined in the next section. A brief history of rocket effects on the ionosphere follows. Section IV covers the Charged Aerosol Release Experiment (CARE) I experiment that used a solid rocket motor burn to inject particulates and high speed molecules into the upper atmosphere. The rest of the paper deals with Space Shuttle OMS burns using a wide range of ground and space-based diagnostics. The future of rocket exhaust experiments is discussed in the final section.

## II. ROCKET BURNS WITH THE IONOSPHERE

Rockets burning in the upper atmosphere produce exhaust that impacts the ionosphere. The composition of rocket exhaust is typically molecules ($H_2$, $H_2O$, $CO_2$, $N_2$, CO) and, for solid propellants, particulates ($Al_2O_3$). The velocity of the exhaust relative to the nozzle is between 2 and 3 km/s. The rocket itself can be moving a speed up to 8 km/s or more. The kinetic temperature of the exhaust is low ($\sim$120 K) but heating can occur by collisions with the atoms in the upper atmosphere. The full perturbations of the neutral atmosphere include: 1) snow plow of the ambient species; 2) collisional heating of the neutrals; and 3) chemical reactions with the neutrals particularly atomic oxygen leading to oxidation. The reactions with the plasma in the ionosphere include ion-molecule charge exchange, electron-ion recombination, and optical emissions from chemiluminescence.

The motion of rocket exhaust in the upper atmosphere is difficult to describe computationally because the expansion starts out with fully collisional fluid flow when the cloud mean free path is much less than the plume diameter and eventually expands to a point where the exhaust cloud density is greatly reduced so it is porous to ambient neutral molecules. The back-
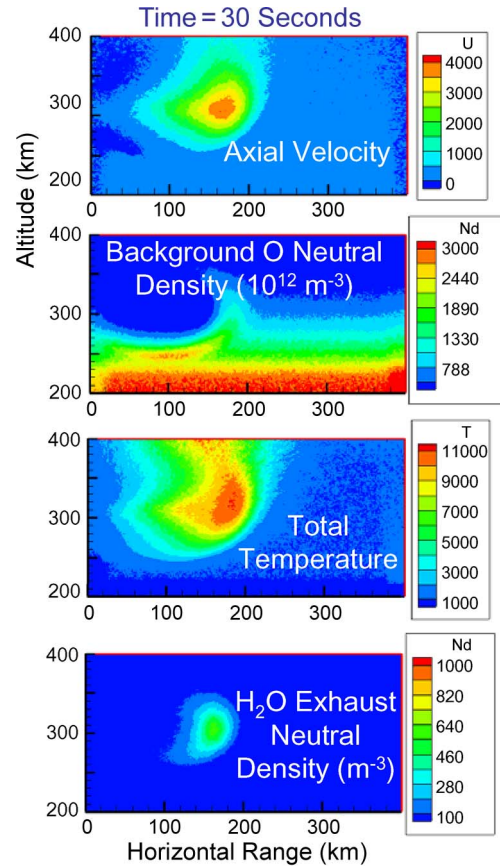


Fig. 2.   Water vapor cloud simulated with the NRL DSMC model. The densities come from a 10-s burn of the Space Shuttle OMS engine moving at 7.7 km/s with a ram burn.

ground neutral atmosphere is picked up by the exhaust leaving a depleted density region behind the exhaust gas "snow plow." After the injected molecules lose their initial momentum, they diffuse through the background.

The modeling for the transport of exhaust plumes is provided by a 2-D, time-dependent direct simulation Monte-Carlo (DSMC) code developed at NRL [2]. Using 54 million particles, streaming exhaust species such as $N_2$, $H_2O$, $H_2$, and $CO_2$ are allowed to interact with background O, $O_2$ and $N_2$ gases. The flowfield is divided into a matrix of 800 horizontal by 400 cells with four subcells for collision sampling. The outputs of the code are the density of each species, the three components of velocity, and the translational and rotational temperatures in each cell. The unique features of the DSMC code are: 1) it covers a wide altitude range of 200 km and 2) the background neutrals are initialized with a realistic density reduction with altitude [2]. A simulated dual OMS burn in the ram direction is shown in Fig. 2 for an exhaust velocity of 3.07 km/s and an exhaust flow rate of $5 \; 10^{26}$ molecules/s for 10 s.

A wide range of waves are produced by the sudden introduction of hypersonic neutrals into the upper atmosphere. Neutral acoustic waves and propagating acoustic gravity waves can be launched by an engine burn [3]. Plasma waves and plasma turbulence will be generated in the ionosphere during an engine burn. Some of the plasma waves that do not propagate are in the class of electrostatic oscillations. The electromagnetic waves trigged in the ionosphere by an engine burn can propagate
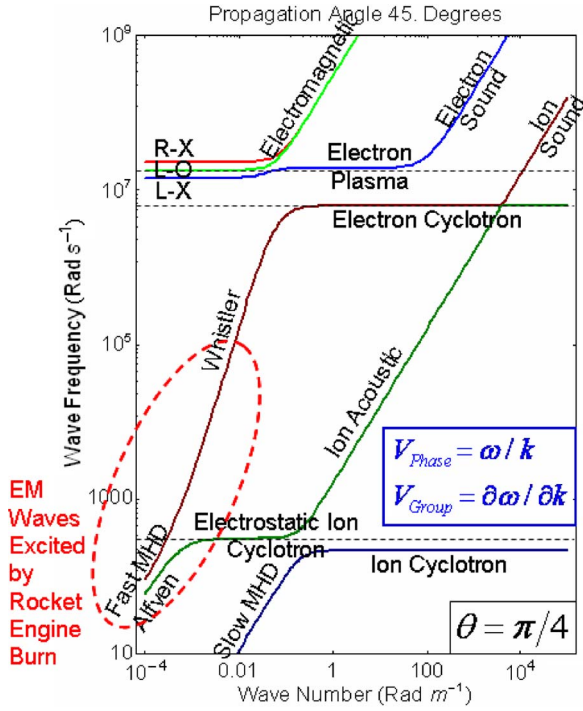
Fig. 3. Waves in a fluid plasma for oblique propagation.

large distances. Irregularities in both the neutral atmosphere and plasma layer can be produced by a rocket engine burn.

The six plasma wave branches derived from the plasma dispersion relation are shown in Fig. 3. The slope of the lines in the $\omega$ versus k diagram gives the group velocity. The horizontal parts of the curves such as for the electrostatic ion cyclotron, electron cyclotron, and electron plasma waves have zero group velocity and consequently do not propagate. The sloped portions of the curves have a sufficient group velocity to travel from a source region to remote sensors on satellites or on the ground. The electromagnetic "light" waves, shown as a light green curve, propagate at the speed of light c. Other modes such as whistler, fast MHD, and Alfven travel at speeds much larger than the sound speed but still only a fraction of c [4]. These waves may be excited as hypersonic exhaust molecules travel though the ionosphere. For propagation perpendicular to the magnetic field, other wave modes are present such as the lower and upper hybrid waves, and the ion and electron Bernstein modes [4].

A wide range of fluid plasma waves are natural modes of the ionosphere. The set of equations that describe plasma wave generation by rocket exhaust in the ionosphere are the continuity equation, the momentum equation, the energy equation, and Maxwell's equations with Hall terms included

$$\frac{\partial n}{\partial t}+n_0\nabla\cdot\mathbf{v}=0, \frac{\partial \xi}{\partial t}=\mathbf{v},$$
$$\frac{\partial \mathbf{v}}{\partial t}=-\frac{\nabla(nKT)}{n_0 m_i}+\frac{(\nabla\times\mathbf{B})\times\mathbf{B}_0}{\mu_0 n_0 m_i}+\nu_{in}(\mathbf{v}_n-\mathbf{v})$$
$$\frac{\partial nKT}{\partial t}-\gamma k T_0\frac{\partial n}{\partial t}=0,$$
$$\mathbf{E}+(\mathbf{v}+\mathbf{v}_H)\times\mathbf{B}_0=0, \frac{\partial \mathbf{B}}{\partial t}=-\nabla\times\mathbf{E},$$
$$\mathbf{v}_H=-\frac{\mathbf{J}}{n_0 e}, \mathbf{J}=\frac{\nabla\times\mathbf{B}}{\mu_0} \tag{1}$$

where n is electron density, $\xi$ is displacement, v is plasma velocity, T is plasma temperature, E is electric field, J is current and B is magnetic field [5]. $\mathbf{V}_H$ is a term representing Hall transport addition to MHD which includes the effects of electrons. Variables with subscript "0" are for ambient medium. This system is driven by the ion neutral collision frequency, $\nu_{in}$, and the neutral velocity vector $\mathbf{v}_n$. A wave equation for the plasma displacement is derived from (1) and written as

$$\frac{\partial^2\xi}{\partial t^2}+\nu_{in}\frac{\partial \xi}{\partial t}-C_S^2\nabla(\nabla\cdot\xi)-C_A^2\left(\nabla\times\frac{\mathbf{B}}{B_0}\right)\times\mathbf{b}=\nu_{in}\mathbf{v}_n$$

$$\frac{\partial}{\partial t}\left[\frac{\mathbf{B}}{B_0}-\nabla\times(\xi\times\mathbf{B})\right]+\frac{C_A^2}{\Omega_i}\left[\nabla\times\left(\nabla\times\frac{\mathbf{B}}{B_0}\right)\right]\times\mathbf{b}=0$$

$$\text{where}\quad \mathbf{B}_0=B_0\mathbf{b}, C_S^2=\frac{\gamma k T_0}{m_i}, C_A^2=\frac{B_0^2}{nm_i}, \Omega_i=\frac{eB_0}{m_i}. \tag{2}$$

The $\nu_{in}\mathbf{v}_n$ term is directly associated with the exhaust plume with increased ion neutral collisions because of the added neutral concentration from the plume and increased velocity because of the hypersonic flow of the exhaust. This term can represent excitation by neutral collisions that transfer energy to the ions with and without charge exchange. The low-frequency modes shown by the bottom half of Fig. 3 are all described by (2).

The excitation of kinetic waves occurs with the formation of nonequilibrium ion velocity distributions. The neutral velocity distribution is given by the first equation in (3). When this neutral particle beam passes through a plasma, charge exchange can convert a hypersonic neutral into a hypersonic ion [6]. These pickup ions, given by the second distribution function in (3), will be guided along the magnetic field lines with gyro motions perpendicular to **B** and beam motion along the magnetic field. This charge-exchange process causes the formation of an ion ring-beam distribution function [7]. A wide variety of ion plasma waves have been attributed to this nonequilibrium distribution in a pickup ion plume [7]–[9]

$$f_n(v_x, v_y, v_z; v_{x0}, v_{y0}, v_{z0})$$

$$=\frac{N_R}{(2\pi v_n^2)^{3/2}}\text{Exp}\left[-\frac{|\mathbf{v}-\mathbf{v}_{n0}|^2}{2v_n^2}\right]$$

$$f_i(v_r, v_z; v_{r0}, v_{z0})$$

$$=\int_0^{2\pi} f_n(v_r\text{Cos}\phi, v_r\text{Sin}\phi, v_z; v_{r0}\text{Cos}\alpha, v_{r0}\text{Sin}\alpha, v_{z0})d\alpha$$

$$=\frac{N_R}{v_n^3\pi^{3/2}}\text{Exp}\left[-\frac{v_r^2+v_{r0}^2+(v_z-v_{z0})^2}{v_n^2}\right]I_0\left(\frac{2v_r v_{r0}}{v_n^2}\right). \tag{3}$$

Solid rocket motors produce dust particles. Charged dust can be formed with electron attachment in the ionosphere by the simple reaction

$$Al_2O_3\text{Dust}: Al_2O_3+e^-\rightarrow Al_2O_3^-. \tag{4}$$
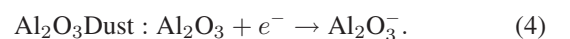
The subsequently produced dusty plasma beam can pass through the ionosphere leaving a trail of dust acoustic waves

TABLE I
EXHAUST MOLECULE REACTIONS WITH $O^+$

| Species | CO | $CO_2$ | $H_2$ | $H_2O$ | $N_2$ |
|---|---|---|---|---|---|
| **Mole Fraction** | 0.050 | 0.122 | 0.241 | 0.274 | 0.313 |
| **Thermal Rate $k_1$ (cm³/s)** | 0.0 | $9.0 \times 10^{-10}$ | $1.7 \times 10^{-9}$ | $2.3 \times 10^{-9}$ | $1.0 \times 10^{-12}$ |
| **Thermal Ion Species (Fraction)** | $CO^+$ (0.00) | $O_2^+$ (0.10) | $OH^+$ (0.36) | $H_2O^+$ (0.55) | $NO^+$ (0.00) |
| **Orbital Rate $k_1$ (cm³/s)** | $6.0 \times 10^{-11}$ | $6.0 \times 10^{-10}$ | $1.7 \times 10^{-9}$ | $2.4 \times 10^{-9}$ | $3.0 \times 10^{-10}$ |
| **Orbital Ion Species (Fraction)** | $CO^+$ (0.00) | $CO_2^+$ (0.06) | $OH^+$ (0.33) | $H_2O^+$ (0.53) | $NO^+$ (0.00) |

[7], [10], [11] or ion acoustic and lower hybrid waves in its wake [12]–[14]. Finally, The affect of these waves on the radar signals was the primary objective of the CARE described below.

In addition to plasma waves, enhanced neutral flow can produce field aligned density irregularities. Using the fluid equations listed in equation group (1), a gradient drift instability can be excited by the fast motion of neutrals through the ionosphere. This instability has been used to explain the formation of field aligned irregularities (FAI) from chemical releases of easily ionizable materials such as barium [15]. By a similar process, the high energy deposition of hypersonic exhaust into the ionosphere can produce striations in the plasma that can be detected remotely with radar scatter. The coherent scatter from these structures is described in Section V-B2.

Visible emissions can be excited by rocket engines burning in the ionosphere through reactions with the atomic oxygen ion. An exhaust molecule charge exchanges with an atomic ion in the ionosphere to produce a molecular ion. This ion rapidly recombines with an electron to produce neutral dissociation products in excited states. The electronic states relax yielding photons that can be observed in terms of artificial airglow. An example of this process from diatomic hydrogen in the F-region is given by the reactions

$$H_2 + O^+ \rightarrow OH^+ + O, OH^+ + e^- \rightarrow O^* + H$$

$$O^* \rightarrow O + h\nu (630.0 \text{ nm and } 557.7 \text{ nm}) \tag{5}$$
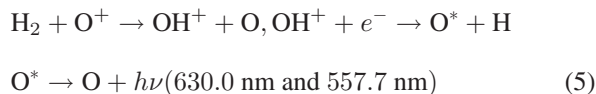
where the excited oxygen produces measurable emissions in the red line and green line of atomic oxygen. The rates for a number of ion-molecule reactions are given in Table I for common exhaust product species. Both the rate constants and the produce ions are affected by the injection speed.

In summary, the transient plume of exhaust from a rocket motor burning in the ionosphere produces a number of unique signatures capable of being detected by sensors in space and on the ground. The hypersonic exhaust vapors can excite a wide range of plasma waves by both fluid and kinetic processes. Electrostatic, nonpropagating waves can be detected with electric and magnetic field sensors flying through the exhaust

plume. The electrostatic waves as well as exhaust-driven field aligned plasma irregularities can be detected by radar scatter. A radar pulse Bragg scatters off the irregularity components that have a wavelength which is 1/2 the probing radar wavelength. The motion of the waves or (FAI) introduces Doppler frequency shifts in the scattered radar signal. Electromagnetic, propagating waves can be remotely detected if the wave receiver is in the propagation direction of the wave ray path. A satellite or ground receiver may be able to receive an electromagnetic pulse (EMP) from the engine burn in the ionosphere. The shape of the pulse contains information about the operation, location, and thrust of the rocket motor. Optical emissions by sunlight scattered from particulates in an exhaust plume as well as fluorescence from resonantly scattered sunlight can be used to locate rocket exhaust plumes. If the plume is fired into the ionosphere at night, chemiluminescent reactions with ion-molecule charge exchange followed by electron-ion dissociative recombination yields a long-lived glow that can be observed from ground or space.

To test these remote sensing techniques, the Naval Research Laboratory (NRL) conducted a series of experiments with the dedicated firing of rocket motors in the ionosphere. The next sections discuss the results of these experiments for: 1) the CARE launch from Wallops Island, Virginia in September 2009; 2) the series of 15 Shuttle Ionospheric Modification with Pulsed Localized Exhaust (SIMPLEX) experiments; and 3) the two Shuttle Exhaust Ion Turbulence Experiments (SEITE). Before discussing these experiments in detail, a review of previous exhaust interactions with the ionosphere is presented.

## III. 50 YEARS OF IONOSPHERIC MODIFICATION BY ROCKET EXHAUST

Since the early launches of rockets into space, ground and *in situ* observations have been made of disturbances produced by rocket exhaust. The 17 February 1959 launch of the Vanguard II rocket left a hole in the ionosphere that was measured using a ground-based ionosondes. The ionosonde record produced "satellite traces" from oblique echoes along with the primary record of the F-layer profile. The time series of ionograms were interpreted to yield the electron density contour plot shown in Fig. 4 [16]. The explanation was given that the exhaust cloud "punched" a hole in the ionosphere. Subsequent observations by the NRL of an ionospheric hole left in the wake of a rocket exhaust burn were recorded using the Faraday rotation of linearly polarized transmissions to detect a reduction in total electron content (TEC) [17].

It was not until the launch of Skylab I in 1974 that the role of chemical reactions was fully appreciated. Mendillo *et al.* [18] reported that for a radius of 1000 km, the F-layer electron densities were significantly reduced after the passage of the Saturn V rocket that placed Skylab I in orbit. This paper introduced the importance of reactions like (5) above to produce an long lasting, ionospheric hole by ion-electron recombination.

NASA sponsored a series of burns during the SpaceLab 2 Mission for the Ionospheric Depletion Experiments (IDE). After launch of the Challenger on 12 July 1985, seven dedicated firings of the Space Shuttle orbital maneuver subsystem (OMS)
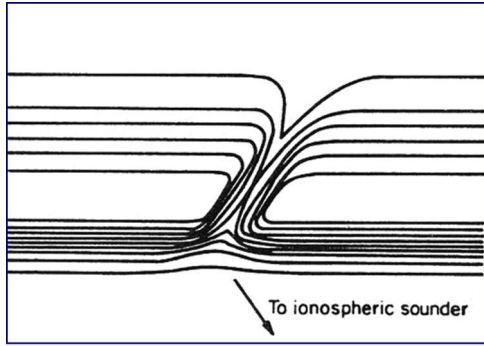
Fig. 4. Reconstructed image of an ionosphere hole produced by the Vanguard II launch in 1959. The F-Layer electron density contours are disturbed by the passage of the burning rocket through the peak of the layer.
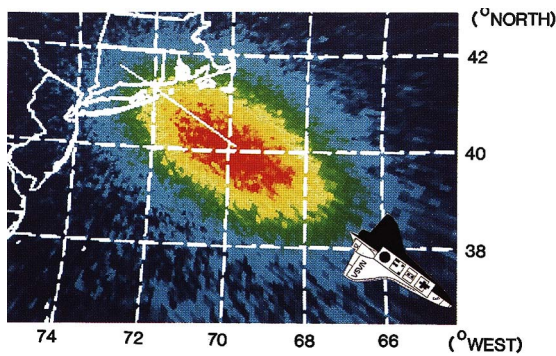


Fig. 5. 630.0-nm emission cloud from the Spacelab 2 Burn Over Millstone Hill, MA on 29 July, 1985.
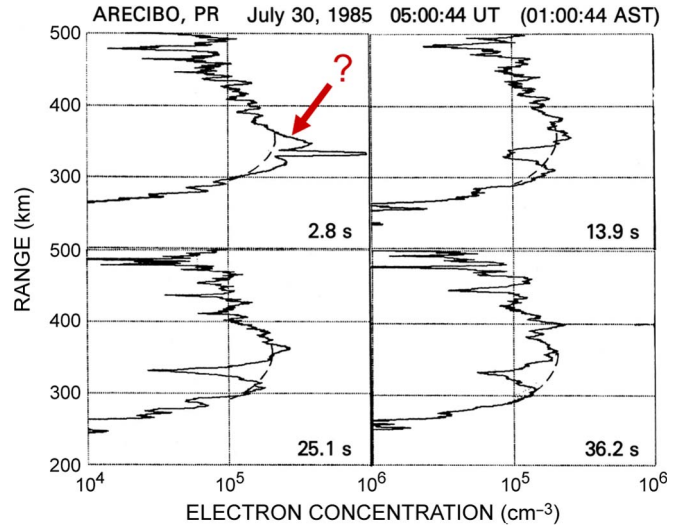


Fig. 6. Sequence of electron backscatter profiles showing the effects of an OMS burn on the 430-MHz radar at Arecibo, Puerto Rico.



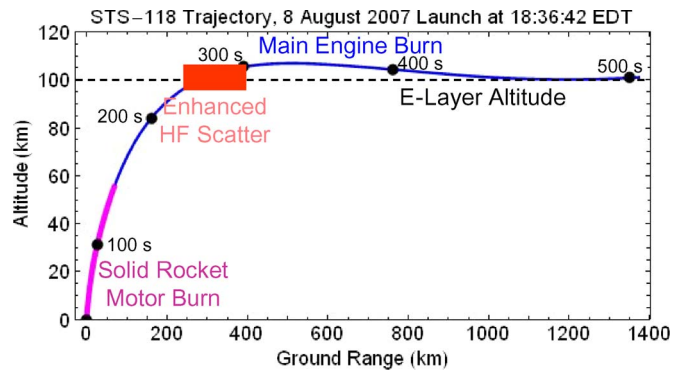Fig. 7. Trajectory of Solid Rocket Booster and Main Engine burns of Space Shuttle Endeavor for STS-118.

engines were conducted over ground radar observatories. The results of these experiments were published in a number of papers [19]–[23]. The largest IDE burn occurred off the coast of Massachusetts to be observed by the Millstone Hill radar. The optical emissions produced by this burn are shown in Fig. 5 showing 40-km downstream slip of the airglow cloud from the location of the exhaust deposition region [19].

Another Spacelab 2 IDE burn took place over the incoherent scatter radar (ISR) at Arecibo, Puerto Rico. With its 300-m diameter dish reflector, Arecibo has the highest resolution system for measuring the ionosphere near 430 MHz. The Arecibo IDE burn produced a localized ionospheric hole that that was preceded by a region of enhanced backscatter on the top and bottom of the release altitude (Fig. 6). Speculation by Bernhardt *et al.* [22] was that his initial region of enhanced radar reflection was caused by exhaust induced turbulence. The charge exchange ions produced by reactions line (5) are created with hypersonic velocities. The streaming of these ions through the plasma trigger kinetic instabilities yielding low-frequency ion acoustic (Fig. 3) and lower hybrid waves. One-half minute after the OMS burn termination, the turbulent echoes are gone, and the ionospheric hole in the profile drops with altitude. This was attributed to a drift of the magnetic flux tube containing the depleted electron densities drifting over the radar beam with a falling intersection altitude.

Subsequent observations have been made by a number of experimenters using GPS measurements of TEC to detect rock-

ets burning in the ionosphere. Mendillo *et al.* [24] reported on the last Titan launch from the U.S. burning off the East Coast. Ozeki and Heki [25] provided measurements of the large ionospheric hole produced by the North Korean launches of the Taepodong-1 on 31 August 1998 and Taepodong-2 on 9 April 2009.

The main engine of the Space Shuttle shuts off at about 100-km altitude. During its 512 s burn, it releases $256 \times 10^3$ kg of exhaust at a flow rate of 500 kg/s. The trajectory of the STS-118 launch is shown in Fig. 7. The solid rocket motors at launch terminate at about 55 km well before they enter the ionosphere. The E-layer, however, resides near 100-km altitude, and the main engine burns can create artificial Sporadic-E layers.

To observe the formation of the Sporadic-E layers, the NRL set up an HF receiver in Ft. Stewart, GA to receive HF backscatter from the relocatable over the horizon radar at Chesapeake, VA. Between 250 and 320 s after the launch of STS-118, a spread Doppler echo with a frequency range of over 20 Hz was recorded from about 100-km altitude (Fig. 8). This Doppler spread, not observed with natural sporadic-E layers, is associated with neutral turbulence in the rocket plume. The radar was operated at 10.205 MHz with 10-km range bins.
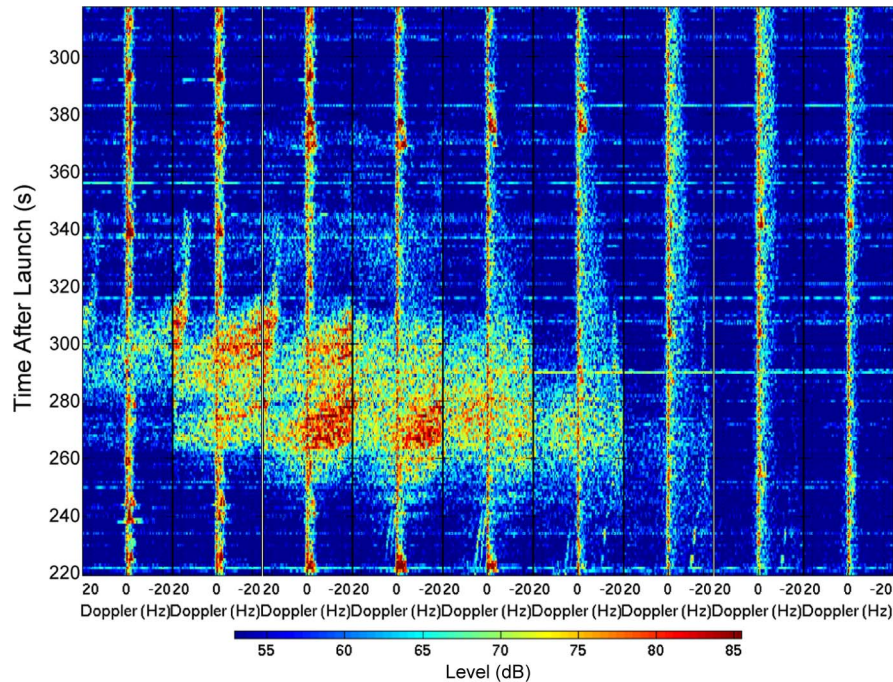
Fig. 8.    Bistatic HF radar scatter near 100-km altitude as the Space Shuttle main engines transit the E-layer at 22:36:26 on 8 August 2007. Each panel is separated by 10 km in range.

After many years of successful observations with ionospheric modifications by rocket launches, the NRL embarked on several programs using both liquid and solid rocket engine burns in the ionosphere. The results of these experiments are summarized in the next sections.

## IV.  CARE I SOLID ROCKET MOTOR EXPERIMENT

The objectives of the CARE are to examine the effect of artificially created, charged-particulate layers on the scatter of UHF, L-Band, and S-Band radars. To accomplish this, a sounding rocket experiment was designed with both a chemical release module and a series of space based and ground-based instruments. Natural dusty plasmas associated with polar mesospheric clouds have been shown to scatter radar echoes with enhanced strength in the frequency range from 30 MHz to 900 MHz [26]. Neutral turbulence in the mesosphere is thought to produce natural irregularities that scatter radar signals. Rocket experiments were designed to test theories of radar scatter from artificially created plasma turbulence in charged dust [10]. The rocket experiment in CARE I used a chemical release from a Nihka motor at 280-km altitude with 111 kg of aluminum oxide ($Al_2O_3$) dust and 200 kg of exhaust molecule vapors. Predictions of the solid rocket plume were performed with flowfield simulations with DSMC [27].

The Nihka motor properties are listed in Table II [28]. The first three stages of the CARE I rocket—Talos, Taurus, and Black Brant V—fired below the ionosphere. The rocket for the CARE I mission was configured as a Black Brant XII with the Nihka motor used as the chemical payload to release dust and molecules into the upper atmosphere. The motor produces 111 kg of aluminum oxide particulates in the 100 nm to 10 micrometer size range with a peak in the size distribution at 1 micrometer. In addition, over 200 kg of molecules are released

TABLE  II
NIHKA MOTOR PROPERTIES

| Quantity | Value |
|---|---|
| Motor Diameter | 0.4384 m |
| Motor Length | 1.92 m |
| Motor Mass | 402.1 kg |
| Fuel Mass | 315.1 kg |
| Ammonium Perchlorate Oxidizer | 69.5% by mass |
| Aluminum Power | 18.0 % by mass |
| HTPB Binder | 12.5 % by mass |
| Nozzle Throat Area | 0.00413 $m^2$ |
| Nozzle Area Ratio | 27.26 |
| Nozzle Exit Diameter | 0.379 m |
| Nozzle Divergence Angle | 19.61 Degrees |
| Throat Gas Temperature | 3523.8 K |
| Throat Gas Pressure | 29.2 atm (29.6 $10^5$ N/m2) |
| Throat Gas Velocity | 1945.9 m/s |
| Gas Specific Heat Ratio | 1.1712 |
| Exit Gas Temperature | 1734.5 K |
| Exit Gas Pressure | 0.207 atm (0.210 $10^5$ N/m2) |
| Exit Gas Velocity | 2835.2 m/s |
| Engine Burn Duration | 17.79 s |
| Thrust | 51.079 kN |
| Total Impulse | 908.77 kN-s |
| Specific Impulse | 2882.51 m/s |
| **Constituent** | **Total Mass** |
| Carbon Monoxide | 69.1 kg |
| Carbon Dioxide | 9.9 kg |
| Monatomic Chlorine | 5.3 kg |
| Hydrogen Chloride | 65.2 kg |
| Hydrogen | 6.6 kg |
| Monatomic Hydrogen | 0.4 kg |
| Water | 30.4 kg |
| Nitrogen | 27.7 kg |
| Aluminum Oxide | 110.6 kg |

by the Nihka for reactions with $O^+$ ion in the F-layer. These molecules charge exchange to produce a charged ion beam. The physics of the beam is discussed in the next section.
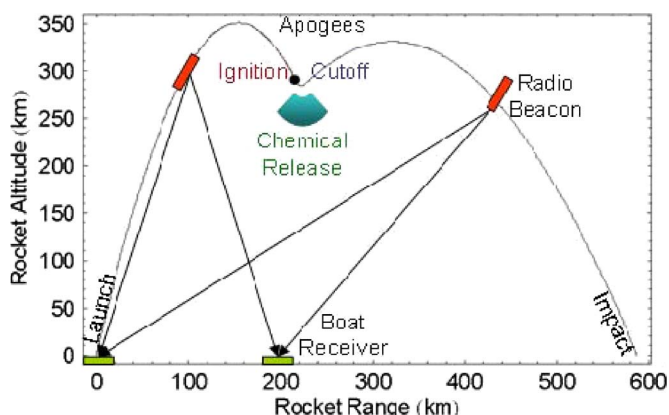
Fig. 9.   Trajectory and radio beacon experiment schematic for the CARE I launch.

The firing of the Nihka fourth stage was delayed to the downleg of the trajectory so that the upward propulsion from the Nihka motor would oppose its downward motion and the chemical release point would stay approximately constant in altitude. The launch of the CARE I mission occurred on 19 September 2009 at 23:46 GMT (18:46 local time) near sunset. The altitude/range trajectory of the rocket is shown in Fig. 9. Between ignition and cutoff of the Nihka motor, the payload hovered near 280-km altitude. The chemical release cloud was injected downward at nearly 3 km/s during the 17.8-s firing of the motor. With this operation, the chemical release of the dust and molecules in the exhaust was concentrated instead of being spread along a stretched-out trajectory of the firing for a typical sounding rocket. Distinguishing the effects of charged dust from hypersonic ions can be made with *in situ* wave observations, ground radar scatter, and optical emissions.

The only instrument on the chemical release payload was a dual frequency (150 and 400 MHz) radio beacon used to measure the integrated electron density between the rocket and the ground. This instrument was also designed to observe amplitude and phase variations of VHF and UHF signals passing through the exhaust plume. The radio beacon transmitted signals to receivers located on the shore and to a ship located below the release (see Fig. 9). This instrument, designated as the Coherent Electromagnetic Radio Tomography experiment, showed the formation of an electron hole in the region of the ionosphere by the exhaust cloud.

The TEC data from the rocket to a ground receiver are obtained from the difference of the phase between the 150 and 400 MHz transmissions. The spin of the rocket is removed from the differential phase signal by recognizing the that TEC is zero before the rocket enters the ionosphere and after it exits the ionosphere on the downleg. Fig. 10-left shows the measured TEC in the vertical direction as a function of rocket altitude before and after the Nihka motor burn. The difference in vertical TEC (VTEC) after the burn represents the amount of electrons removed by the exhaust cloud. Differentiating the VTEC with altitude yields the electron density profile in the stratified regions of the ionosphere (Fig. 10-right). The F-layer profile has a peak density of 2.5 to 3.0 $10^5$ cm$^{-3}$

in agreement with the incoherent scatter profile shown later. The electron density hole has a maximum TEC reduction of $2 \; 10^{15}$ m$^{-2}$ after the release. The radio beacon provides a spatial and temporal view of the chemical release. Details on the radio beacon technique and analysis are given by Bernhardt *et al.* [29].

At the time of the Nihka ignition at 23:46 GMT, the payload was coning at a rate of 0.25 Hz with a coning angle of 8°. The engine thrust operation during the coning caused a midcourse deflection in the trajectory away from the plane of the initial launch. The launch trajectory was south of nominal and that a significant trajectory change occurred because of the mid course burn.

Ground radars were operated at Westford, Massachusetts; Wallops Island, Virginia; and Bermuda. None of the radars saw any enhanced scatter from the dust component of the exhaust. The only radar signature from the experiment was a lingering hole produced in the ionosphere following the ion-electron recombination chemistry given by the example in (5). This measurement was made by the Millstone Hill ISR at 42.6° N latitude and 288.5° E longitude. This UHF radar uses a transmitter with a 2.5-MW peak power feeding a 46-m steerable antenna. The change in the electron density profile along the slanted radar beam is shown in Fig. 11. A comparison of the ISR and radio beacon data shows a similar magnitude for electron density profiles and TEC reduction. The electron density reduction has contributions primarily from exhaust molecule reactions (5). The electron density reduction by charging of dust particles (4) is only important at early times when the cloud has not expanded to more than 1 km in radius.

The optical signature of the CARE I release has been previously reported by Bernhardt *et al.* [30]. The dust particles scattered sunlight to show the conical spread and the residual white cloud with a central hole from the coning motion of the rocket motor. The molecules in the exhaust reacted with the O+ ion to yield molecular ions which after recombination produced an enhancement bright enough to be recorded with a color CCD camera. Spectroscopy was used to determine the major emission species in the release and to identify the ion-electron recombination emission lines (Fig. 12). Small impurities of sodium and potassium are present as well as the strongest AlO lines.

A follow-on CARE II mission is planned for launch from Andoya, Norway. This flight will have a full set of plasma diagnostics to measure the charged dust density, the electron and ion densities, as well as electric fields associated with plasma waves produced by the release. The chemical payload will be changed to use a rocket motor that releases about 100 kg of dust in 2 s, not the 17.8 s of CARE I. Also, an attitude control system will be used to remove the coning of the fourth stage rocket motor. With these improvements, a more dense dust cloud will be formed, and the chances of detecting enhanced radar scatter will be improved. The *in situ* electric field measurements are added to determine the sources of some of the observed plasma waves launched by rocket engines that fire in the ionosphere. These type of observations from liquid fuel engines are described in the next two sections.
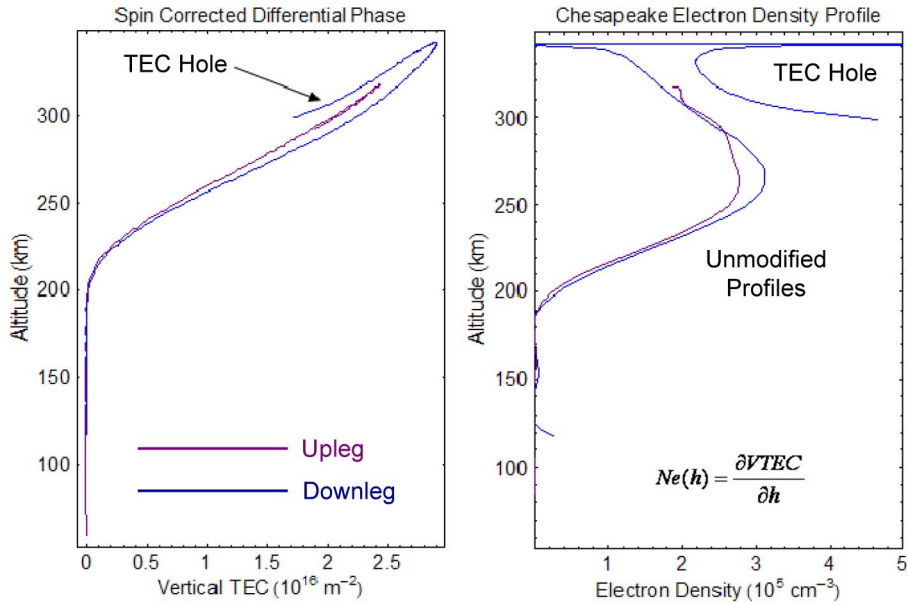
Fig. 10. Total electron content and electron density disturbances by the chemical release determined by radio beacon propagation from the CARE I rocket to a ground receiver.
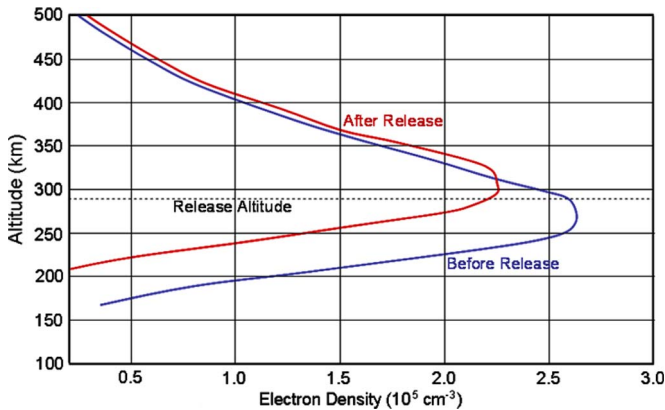


Fig. 11. Electron density profile through the release point of the CARE I rocket obtained by the Millstone Hill ISR on 19 September 2009. The chemical reactions with the exhaust molecules caused the reduction of electron density on the bottom of the F-layer ionosphere. Comparison is good with radio beacon profile shown in Fig. 10.
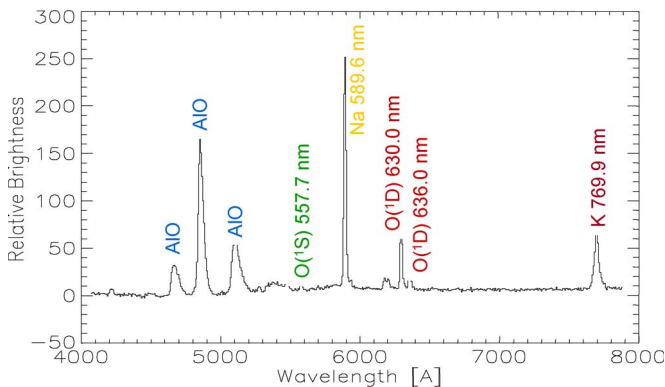


Fig. 12. Spectral lines of the CARE I dust and molecular exhaust release showing oxidation reactions of the aluminum to form the oxide and red-line emissions from excited atomic oxygen produced by electron-ion recombination. The data are from the Boston University spectrograph with a 2-min integration.

## V. SIMPLEX SPACE SHUTTLE OMS BURNS

The next series of experiments with rocket motors firing in the ionosphere are called SIMPLEX. The concept of SIMPLEX is to investigate plasma turbulence driven by rocket exhaust in the ionosphere using ground based radars as sensors. Remote sensing of exhaust flow sources will provide an understanding for the evolution of artificial ionospheric disturbances and allow the development of quantitative models of plasma turbulence. The experiments use dedicated firings of the Space Shuttle OMS engines to perturb the ionosphere over ground diagnostic radar sites. The radar observatories that have been used for SIMPLEX include: 1) the Millstone Hill UHF ISR in Massachusetts; 2) the Arecibo UHF ISR in Puerto Rico; 3) the ALTAIR UHF radar located at the Kwajalein Atoll in the Marshall Islands; 4) the Jicamarca VHF radar in Peru; and 5) the HF SuperDARN radars located at Wallops Island, Virginia. The radar data shows: 1) enhanced backscatter and 2) unusual features in the radar Doppler spectra that have been used to identify the effects of ion beam plasma waves.

During SIMPLEX, other sensors have been employed to augment the radar observations. Radio beacon transmissions from GPS and other satellites have shown reductions in TEC and radio scintillations. Ground cameras have provided optical data from scattered sunlight from exhaust particles and by chemical reaction airglow.

For the SIMPLEX experiments, the OMS engines on the Space Shuttle were fired for 10 or more seconds in the ionosphere and viewed by ground-based radars. The OMS engines provide a flow rate of 10 kg/s ($2.5 \times 10^{26}$ molecules per second) with an exit velocity of 3.07 km/s. When both OMS engines are fired for 10 s, over 1 GJ of energy is deposited into the upper atmosphere. By changing the attitude of the orbiter, the injection velocity can add to, subtract from or be out of plane relative to the 7.7 km orbit velocity of the Space Shuttle. This allowed a wide range of control for speed of exhaust from

Fig. 13. OMS engine plume producing mole fraction percentages of CO (5%), $CO_2$ (12%), $H_2$ (24%), $H_2O$ (27%) and $N_2$ (32%). The OMS exhaust comes from burning monomethyl hydrazine and nitrogen tetroxide fuel.

TABLE III
SIMPLEX EXPERIMENTS IN THE AMERICAS

| Mission | Date | Ignition (GMT) | T (s) | Radars |
|---|---|---|---|---|
| STS-51F SL-2 | 29, 30 July 1985 30 July 1985 | 03:22:00 05:01:36 | 47+ 16 | Millstone Hill Arecibo |
| STS-86 | 4 October 1997 | 20:32:15 | 10 | Jicamarca |
| STS-93 | 27 July 1999 | 04:48:59 | 10 | Arecibo |
| STS-108 | 16 December 2001 | 18:51:37 | 10 | Millstone Hill |
| STS-110 | 18 April 2002 | 17:26:19 | 10 | Millstone Hill |
| STS-118 | 8 August 2007 | 22:36:39 | 10 | Va ROTHR |
| STS-119 | 27 March 2009 | 20:15:43 | 12 | Millstone Hill Wallops SuperDARN |
| STS-128 | 10 September 2009 | 00:08:38 | 10 | Millstone Hill Wallops SuperDARN |
| STS-129 | 26 November 2009 | 14:09:32 | 10 | Arecibo |

TABLE IV
SIMPLEX EXPERIMENTS NEAR KWAJALIEN

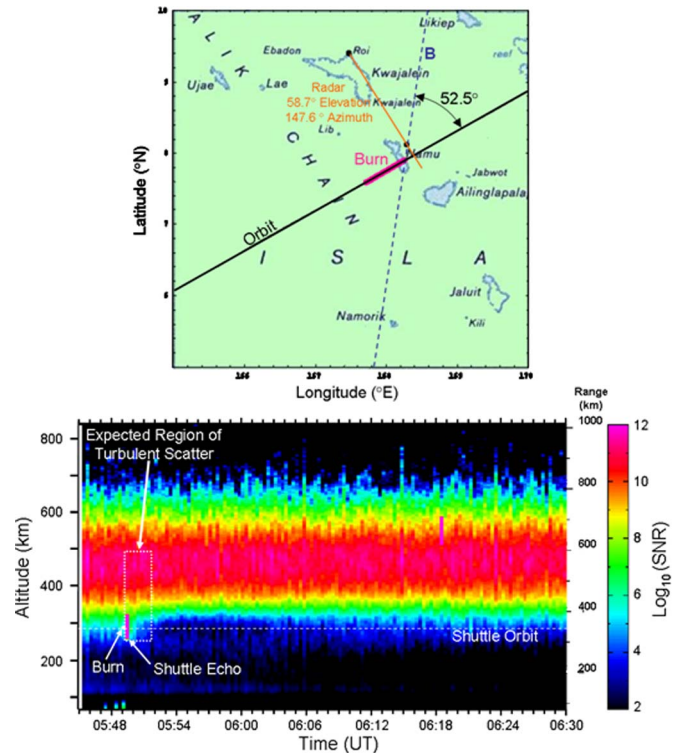| Mission | Date | Ignition (GMT) | T (s) | Sensor |
|---|---|---|---|---|
| STS-93 | 25 July 1999 | 05:49:01 | 10 | ALTAIR |
| STS-120 | 24 October 2007 | 08:05:00 | 10 | ALTAIR |
| STS-122 | 8 February 2008 | 12:42:44 | 13 | AFRL Optics |
| STS-119 | 16 March 2009 | 16:41 | 10 | ALTAIR |
| STS-127 | 17 July 2009 | 14:54:09 | 10 | ALTAIR |
| STS-128 | 29 August 2009 | 20:56:50 | 18 | ALTAIR |
| STS-128 | 30 August 2009 | 20:48:32 | 46.1 | ALTAIR |



Fig. 14. OMS burn along orbit of STS-93 (top) and resulting erosion of the bottomside ionosphere (bottom).

the injection. The exhaust plume has the molecular composition listed in the caption of Fig. 13.

The SIMPLEX experiments were sponsored by the DoD Space Test Program (STP) with collaborations of NASA and the NRL. Table III lists the SIMPLEX experiments that have occurred in the American longitude sector. Most of the dedicated SIMPLEX burns occurred at the end of the Space Shuttle missions when there was extra fuel available after the orbiter had undocked from the International Space Station (ISS). Seven other SIMPLEX experiments listed in Table IV have occurred in the Central Pacific near Kwajalein. Most of these were circularization burns have been reprogrammed to support SIMPLEX. STS-93 had several burns dedicated to SIMPLEX and other plume experiments.

### A. Simplex Experiments Near the Equator

The objectives the experiments at or near the equator were: 1) to study the flow of plasma into the artificial ionosphere hole; 2) to trigger equatorial bubbles; and 3) to employ artificial airglow for enhancement of the viewing of natural irregularities in the ionosphere. The first objective was satisfied during STS-86 with a dual engine burn over the Jicamarca Observatory

in Peru. As has been previously reported in the paper by Bernhardt *et al.* [31], the ionospheric hole recovered more quickly than could be explained using plasma diffusion models.

A chemical release my be used to try to trigger gravitational, Rayleigh-Taylor instabilities in the equatorial ionosphere. [15], [32]. The attempt to trigger a plasma bubble using an OMS burn occurred during STS-93 with a 10-s burn over Kwajalein. The trajectory of the OMS burn is shown by the red line in Fig. 14 (top) along with the path (orange line) of the ALTAIR radar recording UHF backscatter at the end of the burn. The exhaust trail release was 52.5° from the magnetic field direction. This produced an electron density reduction that extended about 50 km perpendicular to the magnetic field lines. The radar recorded the electron density profile modifications shown in Fig. 14-bottom. The engine burn produced a hole on the bottom side of the equatorial layer that is viewed as raising the bottom side in Fig. 14-bottom.
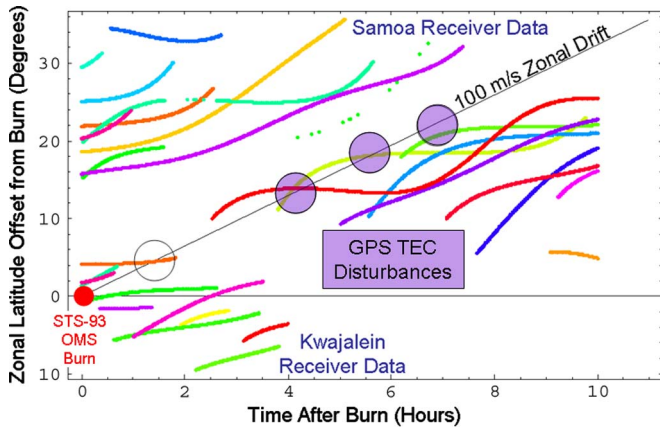
Fig. 15.   Irregularity regions detected by GPS TEC measurements at Samoa for the GPS ground tracks that cross the zonal drift line from Kwajalein. These regions seem to originate with the STS-93 burn observed by ALTAIR.
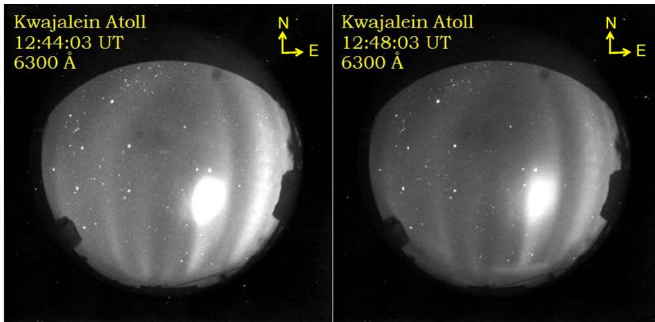


Fig. 16.   Region of enhanced airglow outlining existing ionospheric structures. The exhaust from the OMS engines reacted with the natural field aligned irregularities to produce the structured cloud in the all-sky imager.

The STS-93 burn near Kwajalein occurred at 17:49 local time just before sunset. This is the time that natural plasma bubbles are formed and the artificial hole was designed to be a seed for one of these bubbles. The only diagnostic for the bubble formation was the a GPS receiver in Samoa that measured scintillations and TEC fluctuations. Fig. 15 indicates that the Kwajalein burn from STS-93 may have triggered a disturbance that drifted at 100 m/s eastward to cross the GPS radio paths to the receiver in Samoa. These observations are certainly not conclusive that the OMS burn triggered an equatorial plume disturbance but they are consistent with this hypothesis. The problem with demonstrating cause and effect in an ionospheric modification experiment is proving that a disturbance would not have occurred if the perturbation were absent.

The final example of a successful burn near Kwajalein took place during STS-122 with an OMS burn in a region of strong natural ionospheric irregularities. This burn, which was primarily used to circularize the orbit of the Space Shuttle, was delayed on purpose to put it in view of the science instruments at the Kwajalein Atoll. The UHF ALTAIR radar at Kwajalein was inoperable because of maintenance. The ionosonde showed strong spread-F indicating that equatorial field-aligned irregularities were present. The AFRL ground imager was measuring the red-line (630 nm) airglow with (FAI). When the burn occurred, the exhaust cloud optical emissions were modulated by the natural irregularity structures (Fig. 16). The
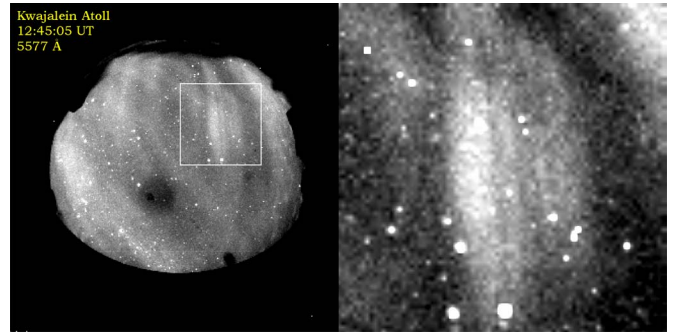


Fig. 17.   All sky image at 557.7 nm with a display of 10-km scale irregularities enhanced by the OMS exhaust artificial airglow.
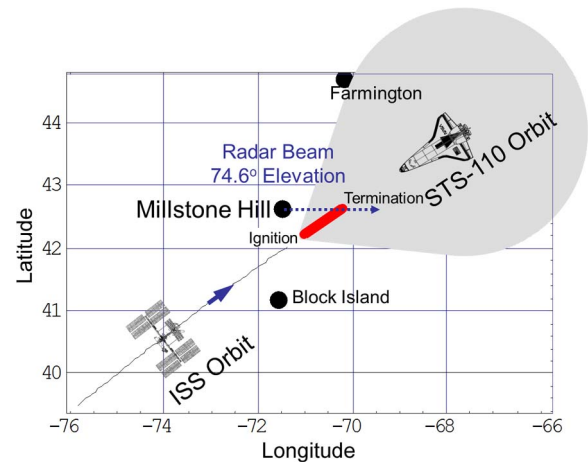


Fig. 18.   Exhaust cloud from the OMS engines crossing the field of view for the Millstone Hill radar.

ion-electron recombination enhanced the contrast of the natural irregularities. An image at 557.7 nm showed features in the natural irregularities that were not visible before the exhaust release (Fig. 17). This experiment demonstrated that exhaust products can be used to better observe irregularity features in the ionosphere.

### B. Simplex Experiments at Midlatitudes

The midlatitude SIMPLEX experiments used ground radars as the primary sensors with support with ground optics and GPS receivers. Most of the SIMPLEX radar observations used incoherent scatter at UHF, but several attempts were made for coherent scatter from FAI at HF.

*1) Incoherent Scatter:* A number of SIMPLEX experiments occurred at midlatitudes using the ISRs at Arecibo, Puerto Rico and Millstone Hill, Massachusetts. The results of the Arecibo experiment during STS-93 were reported by Bernhardt and Sulzer [8]. This paper showed the effects of non-Maxwellian ion distribution functions on the ISR spectra. Both ion temperature enhancements and electron density reductions were observed with the Arecibo 430-MHz radar.

The strongest turbulence in UHF radar backscatter occurred during the STS-110 mission with a 10-s dual OMS burn in field for the Millstone Hill Radar [9]. The 440-MHz radar beam was pointed to the east with a zenith angle for $15.4°$. The OMS
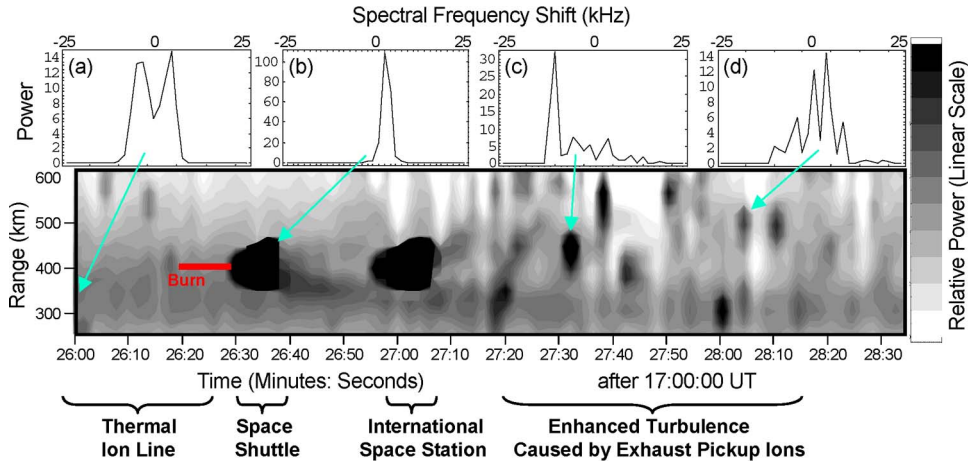
Fig. 19.   UHF radar backscatter from the ionosphere and satellite targets during the STS-110 SIMPLEX flight. The echoes from Space Shuttle and the space station are followed by a 60-s period of enhanced plasma turbulence.

engines were fired in the ram of the Space Shuttle orbit to let the exhaust cloud stream across the UHF radar beam. The geometry of the SIMPLEX STS-110 experiments is shown in Fig. 18. The radar beam was offset from the orbit of STS-110 to prevent main-lobe echoes from either the Space Shuttle or the ISS.

The radar observations of the STS-110 burn provided measurements of strong plasma turbulence. Before the burn, the standard ion-line spectra were obtained with the Millstone Hill radar [Fig. 19(a)]. The peaks of ion line are at the ion acoustic wave frequency corresponding to the 1/2 wavelength (34 cm) Bragg scattering by the radar. Next, the hard target echoes from the Space Shuttle and the ISS saturated the radar receiver [Fig. 19(b)]. Between 30 and 120 s after the OMS burn, the ionosphere was broken into patches of enhanced turbulence. The peaks in the spectral features are observed near harmonics of the ion acoustic wave frequency [Fig. 19(c) and (d)]. These features cannot be explained with incoherent scatter from a stable plasma. These enhancements in the range-time-intensity plot shown at the bottom of Fig. 19 are a series of false targets that are only the result of enhanced scatter from exhaust plasma turbulence. The source of the instabilities may be supersonic pickup ions streaming through the ambient plasma leaving a trail of nonlinear ion acoustic waves [9]. See the next section for follow-on experiments using *in situ* plasma wave and density probes to determine the sources of the observed plasma turbulence.

A comprehensive experiment was conducted during STS-128 with a 10-s OMS burn dedicated to modify the ionosphere over Millstone Hill, Massachusetts. The Space Shuttle was flying at 340-km altitude above the F-layer peak of 250-km altitude. The OMS engines nozzle was oriented 45° downward from the orbit track forcing the exhaust gasses to impact the topside of the F-layer. This flow condition was simulated using the NRL DSMC Model described by Kaplan and Bernhardt [2]. The results of this calculation are shown in Fig. 20 with the exhaust cloud passing over the Millstone Hill radar beam.

Ground cameras were set up near Millstone Hill for observations of sunlight scatter from the burn and the recombination emissions represented by (5). The release occurred at dusk so
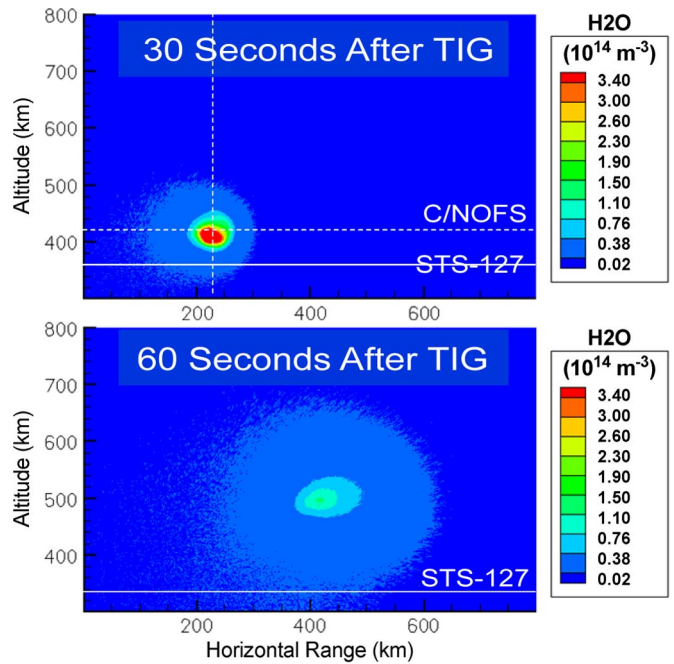


Fig. 20.   Neutral water molecule flow after the injection of OMS exhaust from a 10-s burn. The nozzle of the OMS engines was tilted down by 45°. The burn was times intersect the Millstone Hill radar at 275-km altitude.

the exhaust plume was illuminated by the sun, but the cameras on the ground were in darkness. The burn lasted for 10 s starting at 00:08:38. An image take 7 s into the burn is shown in Fig. 21-top though a 557.7-nm filter. The exhaust flow closely follows the predictions of the DSMC model.

The hypersonic exhaust cloud from the OMS engines was placed along a trajectory to cross the Millstone hill radar beam as shown in Fig. 20. The charge exchange between the exhaust molecules and the background $O^+$ ions produced molecular ions that were streaming along the magnetic field lines in helical orbits. The gyro motion of the ions coupled with the beaming along **B** produced a ring beam velocity distribution. As explained by Bernhardt *et al.* [6], [8], a central peak is formed in
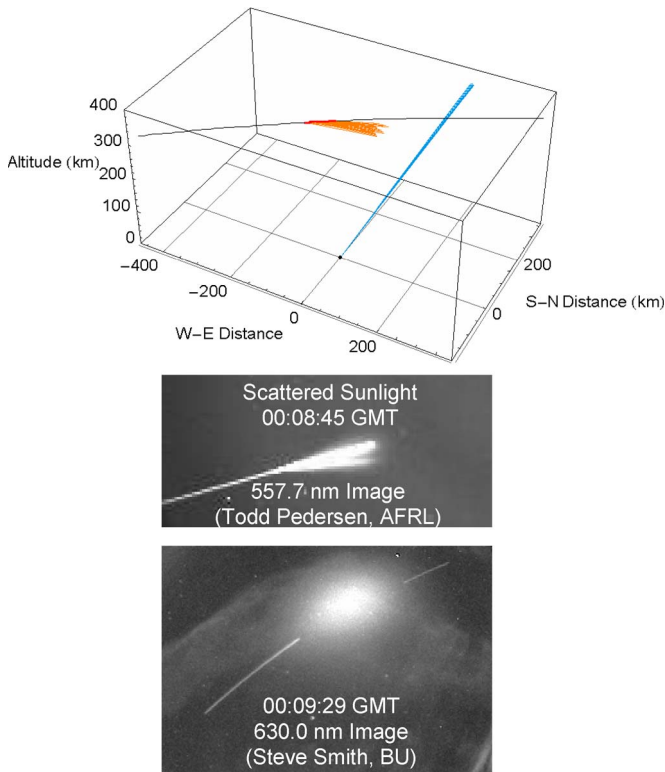
Fig. 21. STS-128 orbit relative to the Millstone Hill radar beam showing the simulated particle trajectories of the exhaust molecules (left). Images of sunlight scattering from the Space Shuttle and OMS exhaust (top right) are similar to the predictions. The interactions with the ionosphere yield emissions at 630 nm (bottom right).

the radar spectrum for the ring distribution. These spectra can be analyzed to yield the velocity of the ions in their gyro motion and the motion along the magnetic field lines. Assuming that all the ions are converted into a ring distribution, the data shown in Fig. 22 shows a ring speed of $v_{r0}$ 0.8 km/s for ions moving along the magnetic field lines at $v_{z0} = 220$ m/s. At these speeds, the plasma velocity distribution is not strong enough to excite instabilities, but the velocity distribution is nonetheless not Maxwellian. This distribution stays in the nonthermalized state for over 20 min. Two processes remove the ion in the ring beam distribution. First, the molecular ions can recombine with electrons to yield neutrals. These neutral are produced in an excited state that yields the airglow cloud shown in Fig. 21 (bottom). Second, if the ions do not recombine, eventually ion–neutral collisions will bring the velocity distribution back to an equilibrium state.

Both SIMPLEX experiments with STS-110 (Fig. 19) and STS-128 (Fig. 22) demonstrated that hypersonic exhaust molecules charge exchange in the ionosphere to yield energetic ion beams that provide a radar backscatter signature lasting from 30 to 90 s to over 20 min. These ions can couple to the electrons affecting both the coherent backscatter with nonlinear ion acoustic waves and the incoherent backscatter affecting Thompson backscatter with non-Maxwellian ions. These kinetic processes can be studied from the backscatter spectra of the UHF radar.

*2) Coherent Scatter:* Fluid instabilities can be excited by the flow of exhaust vapors through the ionosphere. When a large neutral wind blows through a plasma, interchange instabilities can produce (FAI) or striations. To search for large-scale striations driven by the OMS burns, a SIMPLEX experiment was designed to use the SuperDARN HF radar located at Wallops Island, Virginia. This radar operates in the frequency range of 8 to 20 MHz. It is similar to the operational Navy OTH radars with about 1/10th the transmit power. Normally, SuperDARN is used to track natural ionospheric irregularities associated with high latitude auroral disturbances [33]. For the STS-119 SIMPLEX mission, the Wallops Island SuperDARN radar was operated at 11.4 and 14.4 MHz with multiple HF beams pointed to the north viewing the region for a dedicated OMS burn.

The STS-119 OMS exhaust release used a 12-s burn of two OMS engines with a 20-kg/s exhaust flow rage for at total of 240 kg released. The exhaust injection vector had a large component (9.03 km/s) perpendicular to ambient magnetic field. The total hypersonic flow speed was 9.65 km/s. The Space Shuttle orbiting at 356-km altitude was pitched down by $45°$ in the ram direction to force the exhaust to lower altitudes toward the peak of the ionosphere near 240-km altitude. A DSMC simulation of the exhaust cloud showed that the center of the fast neutral cloud reaches an altitude of 280 km before the bulk motion is scatter upward. The topside ionosphere was impacted by a large, supersonic cloud of neutral molecules. This artificial neutral wind probably produced (FAI) in the plasma.

The primary sensor for detection FAI is radar backscatter. Wallops SuperDARN radar had an ideal observation vector to the modified ionosphere. At its operating frequency, Super-DARN can scatter radar signals off 10 to 12 m irregularities. From Wallops Island, the radar elevation angle was $27°$ elevation and the azimuth was $330°$. The line-of-sight distance was 722 km to the interaction region. This line-of-sight geometry was approximately perpendicular to magnetic field with an $102.8°$ to look angle relative to B.

For the STS-119 burn, the 440-MHz Millstone Hill radar supported with observations of the modified ionosphere with its $1.2°$ beam at an elevation angle of $25°$. The UHF radar beam was intentionally placed with a downstream offset from the injection. The burn azimuth was $85.5°$, and the observation azimuth was $82°$ with a nearly perpendicular view ($114°$ Look Angle) relative the earth's magnetic field direction.

The geometry for the two HF radars and the Space Shuttle trajectory are shown in Fig. 23. In addition to Wallops Super-DARN and Millstone Hill, the Virginia Tech Blackstone SuperDARN radar and a GPS receiver were employed to detect changes in the ionosphere. The Blackstone radar did not see any effects, and the GPS receiver saw a drop in TEC immediately after the burn. The Millstone Hill radar was positioned to stare at the F-layer impacted by the exhaust cloud. Fig. 24 shows formation of the persistent ionospheric hole followed by a partial recovery after 25 min. The GPS receiver recorded a 0.45 TECU reduction from the OMS burn.

The primary discovery with the STS-119 SIMPLEX experiment was a region of enhanced HF backscatter from the Wallops SuperDARN radar (Fig. 25). The HF radar was tuned
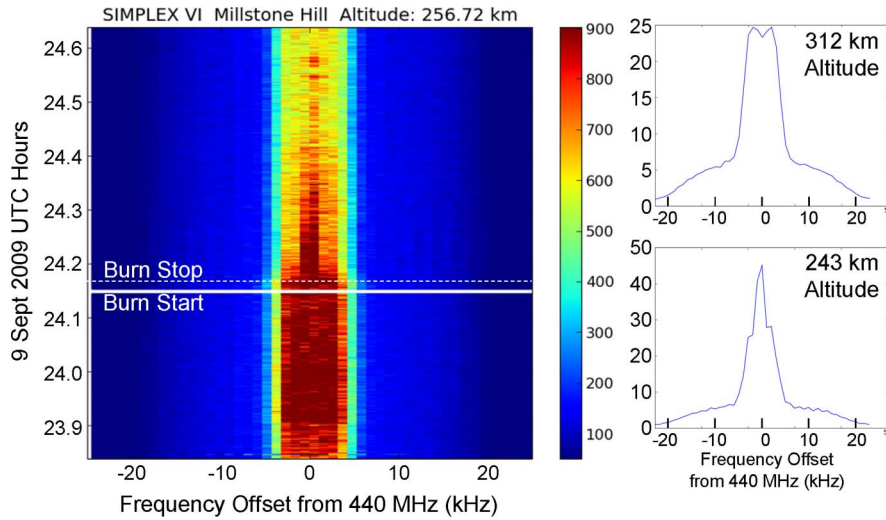
Fig. 22. Incoherent scatter spectra of the thermal ion line (right-top) and ring-velocity ion line (right-left) in the 180 to 400 s after the STS-128 OMS burn near Millstone Hill. The spectrogram (left) shows the transition from thermal ion line before the burn to the nonthermal ion line spectra after the burn.
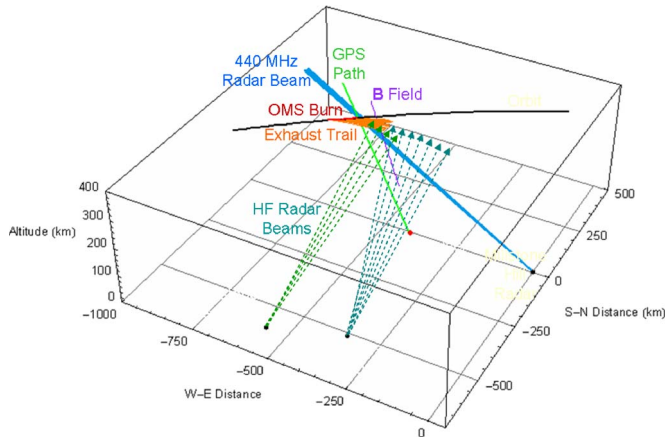


Fig. 23. Radar beams used to monitor the ionospheric effects of the STS-117 SIMPLEX burn.
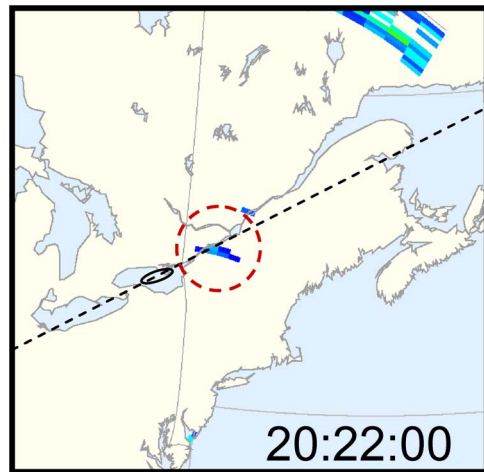




Fig. 25. Enhanced backscatter detected by the Wallops Island SuperDARN radar at ignition time plus 377 s on 27 March 2009. The Space Shuttle ground track is given by the black dashed line. The burn occurred along the portion of the trajectory in denoted by the small ellipse. The radar dashed circle shows the enhanced backscatter region. The large patch of backscatter to the north is ground clutter.

measured this ionospheric disturbance for a period of 40 min after the burn. This disturbance was unique and was not seen near this location with other SuperDARN measurements in two weeks before or after the event. This is the first reported detection of a rocket engine burn in the F-region ionosphere at a range of over 700 km.

## VI. SEITE SPACE SHUTTLE OMS BURNS

Questions on the existence of enhanced plasma turbulence and plasma irregularities in the ionosphere were raised with the successful measurements presented in the previous section. To answer these questions, the NRL proposed a series of experiments where satellites would fly through exhaust plumes. The basic concept for the SEITE mission was to investigate plasma turbulence driven by rocket exhaust in the ionosphere
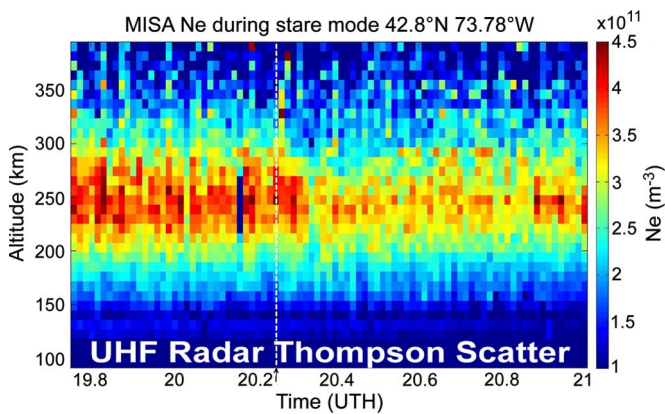
Fig. 24. Electron density determined by analysis of the incoherent scatter radar data during the STS-199 burn over Millstone Hill.

to 14.3 MHz to put the top of the ray path through the region impacted by the rocket exhaust. The backscatter from field irregularities produced in a localized region. The HF radar

TABLE V
SEITE *In Situ* Observation of OMS Burns

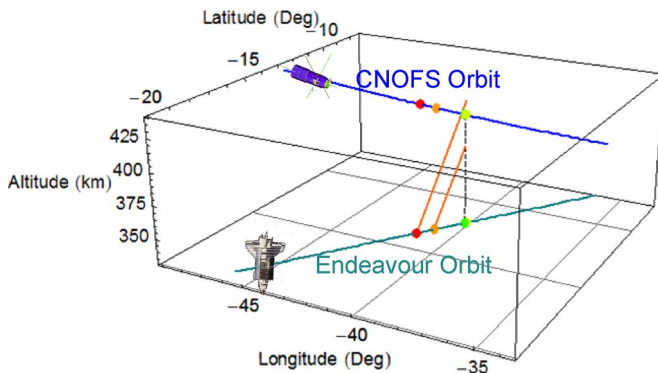| Mission | Date | Ignition (GMT) | T (s) | Sensors | Confirmed C/NOFS Observations |
|---------|------|----------------|-------|---------|-------------------------------|
| STS-127 | 30 July 2009 | 11:03:49 | 12 | CNOFS | IVM, VEFI, PLP, NWM |
| STS-129 | 26 November 2009 | 09:29:14 | 10 | CNOFS | VEFI |



Fig. 26. Space Shuttle (green) and C/NOFS (blue) orbits for the STS-127 SEITE experiment using the sensors on the C/NOFS satellite to measure the effects of a 12-s OMS burn in the ionosphere. The red and orange dots show the positions of the satellites at the start and stop of the burn.

using space-based sensors. Ion and neutral sensors on satellites would provide direct measurements of exhaust flow sources and *in situ* observations of density and electric field disturbances stimulated by the fast neutral flow in the upper atmosphere. The final goal of SEITE was to develop quantitative models of plasma turbulence that can affect tracking and imaging radars.

SEITE provided unique opportunities to fly on-orbit satellite instrumentation through far field plumes from the Space Shuttle OMS engines. One of the satellites selected for these observations include the Air Force Communications Navigation Outage Forecast System (C/NOFS) satellite which is currently in a near equatorial orbit [34]. This satellite has an ideal set of instruments to measure the OMS exhaust effect in the ionosphere. These instruments on C/NOFS include sensors to measure electron density fluctuations, ion densities and drifts, electric Fields, TEC and radio scintillations, neutral flows, and magnetic fields [34]. The two SEITE opportunities are listed in Table V. Both SEITE 1 and 2 provided unique measurements of highly altered neutral and plasma environments resulting from OMS burns in the ionosphere.

## A. SEITE 1 DURING STS-127

The first SEITE experiment occurred during the STS-127 flight of the Space Shuttle Endeavour on 30 July 2009 at 11:03:49 GMT at $-12.7°$ N latitude and $-39.896°$ E longitude near the eastern coast of Brazil. On the last day of the mission, a close conjunction was found between the Space Shuttle and the Air Force C/NOFS satellite. A 12-s burn of both OMS engines was scheduled with the rocket motor nozzles pointed upward to the zenith. With a proper timing of the burn, the rocket plume

was made to cross the 87 km higher altitude orbit of C/NOFS completely engulfing *in situ* plasma sensors with exhaust 30 s after the burn. A diagram of this conjunction is shown in Fig. 26. The burn was initiated when the Space Shuttle, and the C/NOFS satellites were separated by 220-km slant distance. An image produced by solar illumination of the exhaust plume for this burn is shown in Fig. 13.

The NRL DSMC model was used to plan the SEITE 1 measurements. By firing the plume upward, the neutral vapors were transported into regions of increasingly rarified atmosphere and the molecular exhaust cloud was confined to a ball of 60 km after 30 s with H2O densities of $3 \times 10^8$ cm$^{-3}$. The heating of the molecules on the outside of the molecule cloud is shown in Fig. 27 reaching temperatures of 8000 K.

The NRL DSMC model was used to plan the SEITE 1 measurements. By firing the plume upward, the neutral vapors were transported into regions of increasingly rarified atmosphere, and the molecular exhaust cloud was confined to a ball of 60 km diameter after 30 s with H2O densities of $3 \times 10^8$ cm$^{-3}$. The heating of the molecules on the outside of the molecule cloud is shown in Fig. 27 with temperatures reaching 8000 K.

The *in situ* probes on C/NOFS measured the neutral composition and densities, neutral temperatures, ion composition and densities, and ion temperatures inside the exhaust cloud (Fig. 28). The vertical neutral wind went from zero to 3.5 km/s in 6 s. Inside the exhaust plume cloud, 25% of the ions were converted to $CO_2^+$ which was the result of charge exchange of the $CO_2$ exhaust component with ambient atomic ions. The ion temperature was increased by 50% indicating that hot ions were being produced by ambient ion charge exchange with hot neutrals. *In situ* Langmuir probes measurements showed an increase of electron density by about 10% that is attributed to a "snow plow" of plasma in front of the expanding exhaust cloud. All of these measured effects are consistent with the DSMC model of the neutrals followed by charge exchange with ambient ions.

The most spectacular results for the STS-127 SEITE experiment were obtained by the Vector Electric Field Instrument (VEFI) on C/NOFS (Fig. 29). This instrument was operated in a high-speed burst mode from a few seconds before OMS ignition to after the predicted passage of the exhaust cloud. As presented in section 1.2, a wide variety of plasma wave modes can be excited in the ionosphere by a rocket engine burn. The electric field instrument on C/NOFS measured prompt EMPs in the form of an MHD pulse and multiple whistler waves. Two of the whistler waves occurred immediately after the ignition and cutoff of the OMS engines. These may have been excited by transients in the operation of the OMS when the MMH/NTO fuel is flushed from the feed lines [35]. Similar transients have been recorded optically for the Space Shuttle reaction control system motors [35]. About 6 s after the OMS ignition, a large low-frequency pulse was recorded by VEFI. This is thought to be the fast MHD wave that is found in the plasma for frequencies below the ion cyclotron frequency. At the altitude of C/NOFS for the SEITE 1 experiment, the ion cyclotron frequency is 17 Hz. A whistler wave, which is an extension of the fast MHD branch (Fig. 3), is received at the same time as the low-frequency pulse.
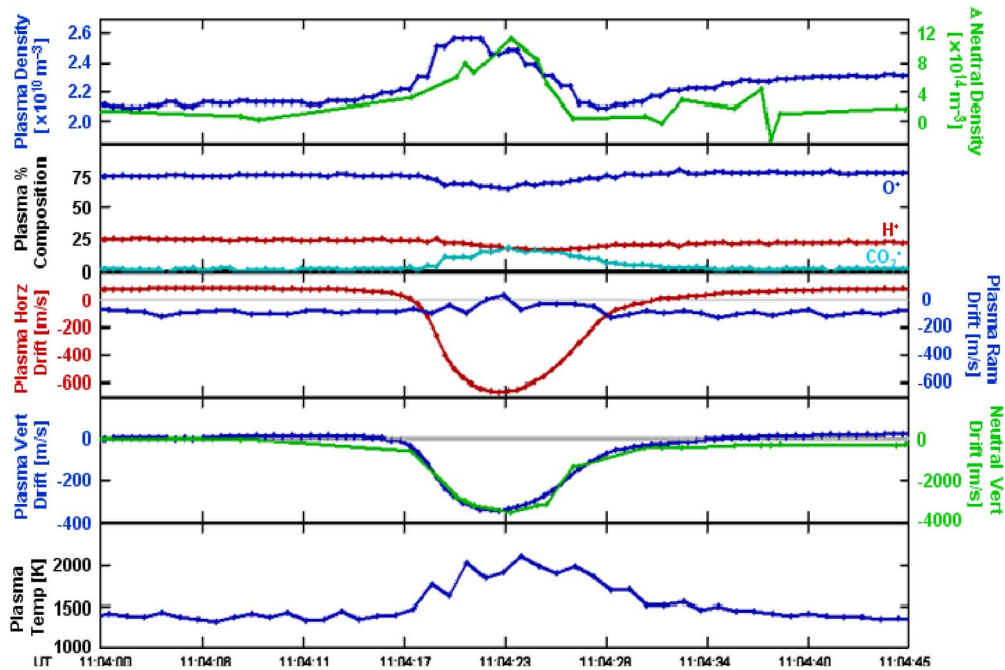
Fig. 27. Elevated neutral temperatures from collisional heating of the background atmosphere computed using the NRL DSMC model. The time of the simulation is when the C/NOFS instruments fly through the OMS exhaust cloud.
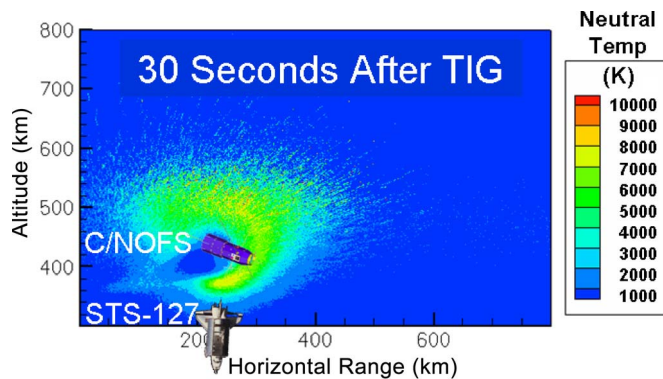


Fig. 28. Measurements of the OMS exhaust disturbance in the ionosphere using the CINDI and PLP instruments on the C/NOFS satellite. The orange line is the time when the satellite is nearest to the center of the exhaust cloud.

Following the initial transient EMPs, a broad band of high amplitude noise dominated the electric-field frequency spectra at C/NOFS. These waves were produced by the high-speed pickup ions in the exhaust cloud. The strength of this noise is the strongest when the C/NOFS satellite is in the center of the cloud. The source of this noise is still under theoretic investigation. It may be ion acoustic waves, but initial kinetic theory using a ring-beam distribution indicates that ion acoustic waves will be strongly damped in the plasma. These waves may also be harmonics of the ion cyclotron frequency related to the ion Bernstein modes.

### B. Seite 2 During STS-129

Based on the unprecedented results from the first SEITE experiment, a second OMS burn was scheduled for the STS-129 flight of the Space Shuttle. SEITE 2 was conducted on 26 November 2009 at 09:29:14 GMT at $-4.3°$ N latitude and

$-14.4°$ E longitude near the west coast of Africa. The Space Shuttle Atlantis was oriented with its OMS engine nozzles pointed upward as with the previous SEITE experiment.

During SEITE 2, the minimum distance between the Space Shuttle and C/NOFS orbits was 134 km. The OMS engines were fired, and it took about 48 s for the exhaust plume to get to the C/NOFS orbit altitude. The slant distance between the orbiter Atlantis and CNFOS at the time of the OMS ignition was 420 km. The C/NOFS satellite came within 50 km of the center of the exhaust cloud so that only the edge of the cloud was sampled by the *in situ* probes.

The VEFI electric field instrument recorded an EMP pulse about 6 s after the OMS ignition, but no whistler modes were observed at the ignition or cutoff times of the burn. A region of high amplitude plasma wave noise was again recorded as CNFOS entered the exhaust cloud. A sample of the electric fields recorded on C/NOFS is shown in Fig. 30. The EMP pulse is much broader than for the previous experiment. As expected, the amplitude of the *in situ* plasma wave noise is much less than for SEITE 1.

### C. Wave Mode Propagation Paths

The propagation of electromagnetic waves from the plume interaction region in the ionosphere can be studied by tracing rays through the plasma from the Space Shuttle source to the to the electric field sensor (VEFI) on the C/NOFS satellite. For computation of ray paths in a plasma, a dispersion equation must be specified with the form

$$D\left[\mathbf{k}, \omega(\mathbf{k}, \mathbf{r}, t), \mathbf{r}\right] = 0 \qquad (6)$$

where $\mathbf{k}$ is the wavenumber vector, $\mathbf{r}$ is the position vector, $t$ is time, and $\omega$ is the wave frequency for the propagation mode
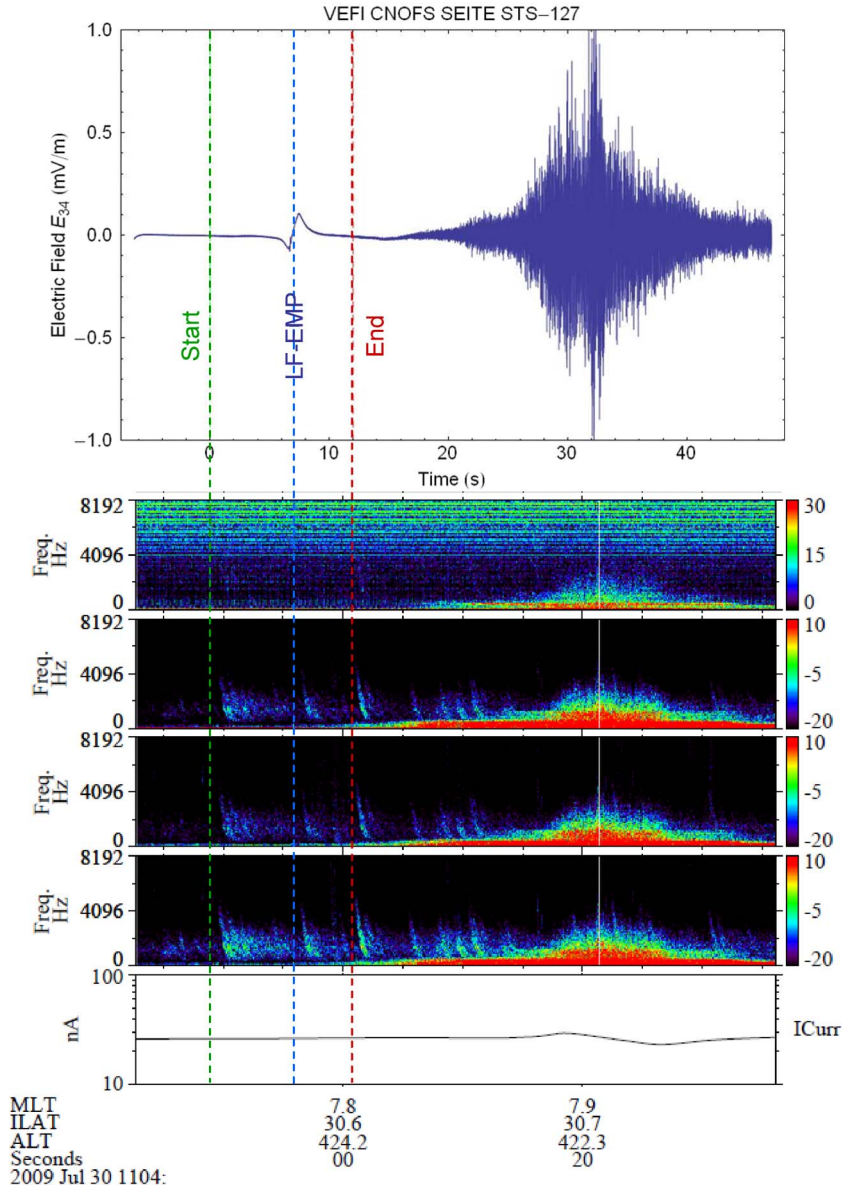
Fig. 29.   Plasma wave measurements obtained with the VEFI instrument on C/NOFS. Frequency dispersed waves called whistlers were observed immediately after the ignition and cutoff of the OMS engine.
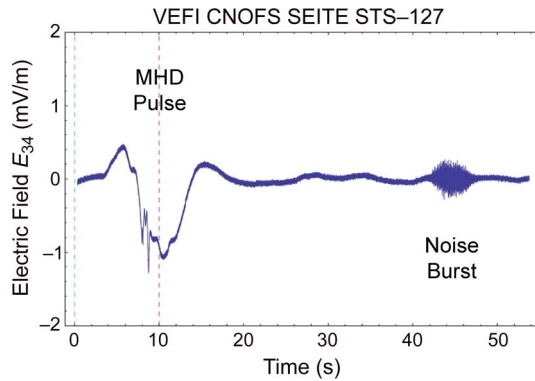


Fig. 30.   Plasma waves excited by the OMS burn during the second SEITE experiment on the STS-129 flight.

in the plasma. The plasma medium is assumed to be stationary during the transit time for the wave propagation. The ray wave normal angle and position is propagated by the differential equations

$$\frac{d\mathbf{k}}{d\tau} = \nabla_{\mathbf{r}} D[\mathbf{k}, \omega, \mathbf{r}], \quad \frac{d\mathbf{r}}{d\tau} = -\nabla_{\mathbf{k}} D[\mathbf{k}, \omega, \mathbf{r}], \quad \frac{dt}{d\tau} = \frac{dD[\mathbf{k}, \omega, \mathbf{r}]}{d\omega} \tag{7}$$

where $\tau$ is the scaled propagation variable along the ray trajectory [36].

The specific form of the dispersion (6) depends on the modes considered for the ray propagation. For the electric field observations, the wave frequencies limited to those much lower than the electron cyclotron frequency. Assuming that the Hall MHD (1) have Fourier time dependences of the form $\exp(i\mathbf{k} \cdot \mathbf{r} - i\omega t)$, a convenient way to write the low-frequency dispersion function is

$$D[\mathbf{k}, \omega, \mathbf{r}] = \omega^2 \omega_{WH}^2 \left(\omega^2 - \omega_{IA}^2\right) - \left(\omega^2 - \omega_{ALF}^2\right) \left(\omega^2 - \omega_{SMHD}^2\right) \left(\omega^2 - \omega_{FMHD}^2\right) \tag{8}$$
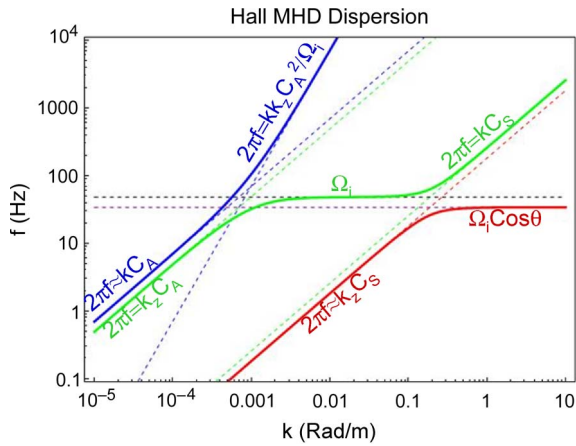
Fig. 31.   Low-frequency plasma wave branches derived from the plasma dispersion equation.

where the whistler, ion acoustic, Alfven, slow magnetohydro-dynamic (MHD), and fast MDH frequencies are defined as

$$\omega_{WH} = \frac{kk_z C_A^2}{\Omega_i}, \omega_{IA} = kC_S, \omega_{ALF} = k_z C_A,$$

$$\omega_{SMHD} \cong k_z C_S, \omega_{FMHD} \cong kC_A$$

with $C_S \ll C_A$ and $k_z = k\mathrm{Cos}\theta$. Dispersion (8) was used to compute the sample dispersion curves for low-frequency plasma wave shown in Fig. 31. Below the ion cyclotron frequency $\Omega_i$, only the fast MHF (blue), Alfven (green), and slow MHD (red) modes exist. Above the ion cyclotron frequency and below the electron cyclotron frequency, the whistler (blue) and ion acoustic modes (green) are supported by the plasma. Near the ion cyclotron frequency, the electrostatic ion cyclotron wave (green) and second ion cyclotron mode (red) are found. All of these waves can be excited by the injection of rocket exhaust into the ionosphere. The group velocity vector, defined as $\mathbf{v}_g = \nabla_{\mathbf{k}}\omega$, has a magnitude given by the slope of the curves in Fig. 31.

Numerical mode ray tracing is used to explain: 1) the presence of the fast MHD wave for both measurements and 2) the absence of whistlers for the SEITE 2 burn and the strong presence of whistlers for SEITE 1. The fast MHD or compressional Alfven wave can propagate in all directions with some refraction in the magnetized plasma that tries to confine the mode in the F-region layer. Rays are traced from the Space Shuttle to the C/NOFS satellite for both experiments in Fig. 32. For the STS-127 experiment, the Space Shuttle was almost directly below the C/NOFS electric field sensor, and the propagation path was nearly straight without much path mixing [Fig. 32 (top)]. The ray paths to C/NOFS were refracted by the topside and bottomside electron density gradients in the F-region causing both dispersion and path mixing to the electric field sensors. These path differences explain the compact N-Wave in the first experiment and the more dispersed wave in the second.

Of the modes excited by a rocket engine firing in the ionosphere, the fast MHD wave is the most likely to be received
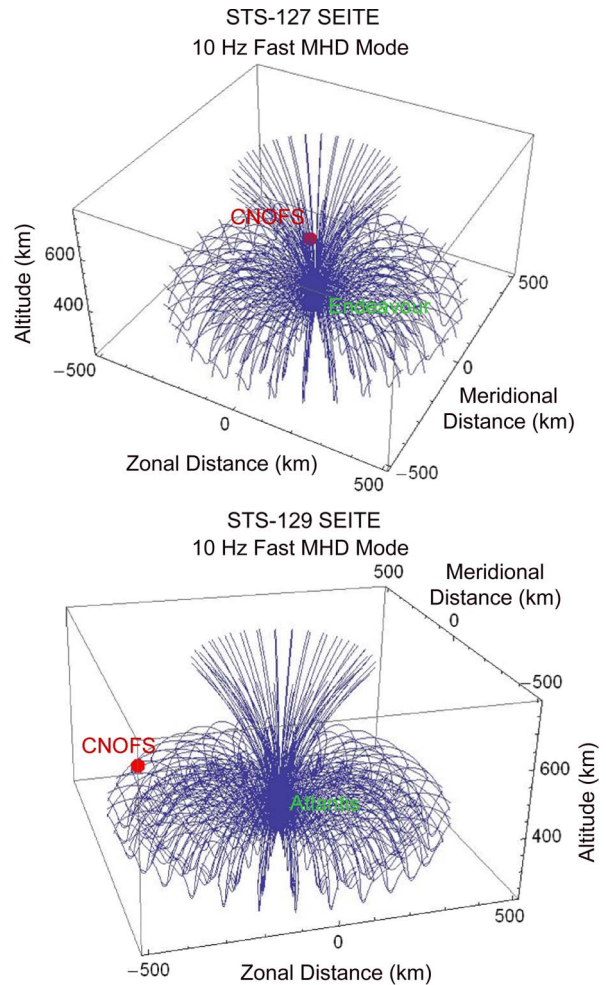




Fig. 32.   Fast MHD ray paths launched by the Space Shuttle OMS burns for SEITE experiments 1 and 2. The STS-127 burn (top) launched compressional Alfven waves directly to C/NOFS. The STS-129 burn (bottom) excited multiple rays that took refracted paths to C/NOFS.

at a remotely located satellite. This mode propagates in all directions with a group velocity given by

$$v_{gFMHD} = \sqrt{C_A^2 + C_S^2 Sin^2\theta} \qquad (9)$$

where $C_A$ is the Alfven velocity and $C_S$ is the ion acoustic speed both defined in (2). The propagation angle ? is relative to the magnetic field direction. In the ionosphere, $C_A \gg C_S$ so the fast MHD wave propagates almost isotropically from the source point. For SEITE 1 and 2, the Alfven speed is estimated to be around 300 km/s.

The energy of the whistler mode, in contrast, travels in a $19.5°$ cone around the magnetic field [4]. Consequently, whistler waves excited by the OMS burn will only be observed if the C/NOFS satellite is within this cone. Using a ray trace code developed at NRL, an isotropic distribution of initial wave normal angles was launched to simulate the ignition point of the OMS engines in a model ionosphere and magnetic field. The background plasma density profile was estimated using *in situ* measurements from the C/NOFS satellite and ground ionosondes. For SEITE 1, the C/NOFS satellite is contained within the cone of whistler-mode rays [Fig. 33 (top)]. For
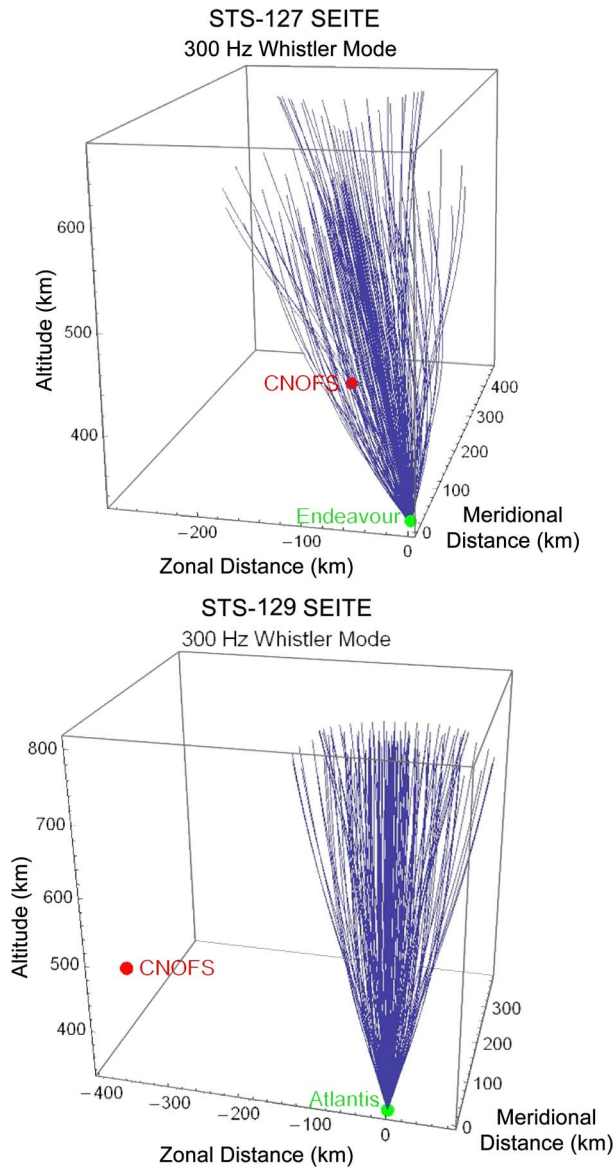
Fig. 33.   Whistler mode ray paths launched by the Space Shuttle OMS burns during SEITE 1 and 2. C/NOFS was positioned (top) in the whistler mode cone for SEITE 1 and (bottom) outside the whistler mode cone for SEITE 2.

SEITE 2, the C/NOFS satellite is well outside the whistler mode propagation cone from the STS-129 orbiter. For whistler mode frequencies well below the electron cyclotron frequency, all the rays follow the same paths with different group delays. The time dispersion shown in the observed spectra (Fig. 29) for the whistler is caused by propagation through the magnetized plasma of the ionosphere. Analysis of this dispersion should provide the range to the source of the disturbance if there is an accurate model of the background plasma.

The second most likely mode to be detected by a rocket burn in the ionosphere is the whistler wave. This wave propagations at a group velocity near 3000 km/s in a 19° half-angle cone around the magnetic field lines. The whistler propagates in both directions along the magnetic field lines. The chance of any satellite being in the whistler cone is less than six%. Dedicated burn experiments such as SEITE 1 can intentionally initiate a

burn when the electric field sensors are in the correct locations for whistler mode measurements.

The Alfven wave mode itself will be launched by a OMS burn, but its propagation is confined to a magnetic field line [3], [4]. The only way that a satellite electric field sensor can see the Alfven wave is to be on the magnetic field line connecting the source region at the time when the wave pulse passes that point.

The SEITE experiments have shown that a large number of electrostatic waves are produced by rocket exhaust neutrals after they are converted into high-speed pickup ions. The pickup ions can either stream along or gyrate around the magnetic field lines. This produces unstable ion velocity distributions which promote the plasma wave growth by instabilities. The ion acoustic, lower hybrid, and ion Bernstein waves that result from the instabilities yield the broadband spectra shown in Fig. 29. These electrostatic waves also produce the enhanced radar backscatter shown in Fig. 19. Radar backscatter responds to electron fluctuations at one-half the radar wavelength. The *in situ* observations record the local strength of electric fields and density fluctuations at all wavelengths. The bulk flow of the exhaust compresses the F-region plasma launching MHD and whistler waves. The high-frequency transients of the OMS engine launch whistlers at the beginning and end of a burn. The large volume of gas interactions induce ionospheric currents that lead to the production of the fast MHD wave which is measured as a low-frequency EMP.

## VII. Summary

Rocket burns in the F-region ionosphere can be the source of a wide range of effects that can be measured with sensors on the ground or on satellites. The ionosphere provides electrons and ions that interact with the exhaust vapors to yield light emissions, (FAI), electrostatic waves, and propagating EMPs. Ground and satellite optical sensors can observe the light emissions. Ground radar transmissions can scatter from the irregularities and electrostatic waves at distances over 700 km. Satellites with electric field sensors can readily detect the space-generated electromagnetic signal from an ionospheric rocket burn. This fast MHD wave propagates in all directions with a speed on the order of 300 km/s.

Rocket exhaust provides an impulse to the space plasma environment used to study a wide range of physical processes. Ion molecule chemistry and electron-ion recombination can be investigated with *in situ* probes flying through the exhaust plume. Satellites such as C/NOFS designed for space weather applications can be adapted for these observations. Numerous kinetic and fluid instabilities in the low-$\beta$, collisionless plasma can be studied with remote and direct sensors. Radar scatter at HF to UHF wavelengths provide ground-based data on the evolution and longevity of these instabilities.

The era for using the Space Shuttle to study the exhaust-plasma interactions in the upper atmosphere is over. The new vehicles designed for transport to the ISS have thrusters that have less than one-tenth the mass flow rate of the Space Shuttle OMS engines. Future large disturbances in the F-Region will be primary launch vehicles that have their rocket motors burning well into the upper atmosphere.

## ACKNOWLEDGMENT

## REFERENCES

[1] J. D. Huba, G. Joyce, and J. A. Fedder, "SAMI2 (Sami2 is another model of the ionosphere): A new low-latitude ionosphere model," *J. Geophys. Res.*, vol. 105, no. A10, p. 23 035, 2000.

[2] C. R. Kaplan and P. A. Bernhardt, "The effect of an altitude-dependent background atmosphere on space shuttle engine burn plumes," *J. Rockets Spacecraft*, vol. 47, pp. 700–704, 2010, DOI:10.2514/1.49339.

[3] R. R. Ahmadov and V. E. Kunitsyn, "Simulation of generation and propagation of acoustic gravity waves in the atmosphere during a rocket flight," *Int. J. Geomagn. Aeron.*, vol. 5, p. GI2 002, 2004, DOI:10.1029/2004GI000064.

[4] D. G. Swanson, *Plasma Waves*, 2nd ed. Bristol, U.K.: Inst. Phys. Publ., 2003.

[5] W. B. Thompson, *Introduction to Plasma Physics*. New York: Pergamon, 1962.

[6] P. A. Bernhardt, "A critical comparison of ionospheric depletion chemicals," *J. Geophys. Res.*, vol. 92, no. A5, pp. 4617–4628, 1987.

[7] P. A. Bernhardt, J. D. Huba, W. E. Swartz, and M. C. Kelley, "Incoherent scatter from space shuttle and rocket engine plumes in the ionosphere," *J. Geophys. Res.*, vol. 103, no. A2, pp. 2239–2251, 1998.

[8] P. A. Bernhardt and M. P. Sulzer, "Incoherent scatter measurements of ion beam disturbances produced by space shuttle exhaust injections into the ionosphere," *J. Geophys. Res.*, vol. 109, p. A02 303, Feb. 2004.

[9] P. A. Bernhardt, P. J. Erickson, F. D. Lind, J. C. Foster, and B. Reinisch, "Artificial disturbances of the ionosphere over the millstone hill radar during dedicated burns of the space shuttle OMS engines," *J. Geophys. Res*, vol. 110, p. A05 311, May 2005.

[10] H. Fu and W. A. Scales, "Nonlinear evolution of the dust acoustic instability in artificially created dusty space plasmas," *IEEE Trans. Plasma Sci.*, doi:10.1109/TPS.2011.218092, 2012, to be published.

[11] A. Mahmoudian and W. A. Scales, "Irregularity excitation associated with charged dust cloud boundary layers," *J. Geophys. Res.*, vol. 117, p. A02304, doi:10.1029/2011JA017204, 2012.

[12] M. Rosenberg, P. A. Bernhardt, and S. E. Clark, "Excitation of ion waves by charged dust beams in ionospheric aerosol release experiments," *Planet. Space Sci.*, vol. 59, no. 4, pp. 312–318, Mar. 2011.

[13] H. Fu and W. A. Scales, "Nonlinear evolution of the ion acoustic instability in artificially created dusty space plasmas," *J. Geophys. Res.*, vol. 116, p. A10315, doi:10.1029/2011JA016825, 2011.

[14] M. R. Bordikar and W. Scales, "Lower hybrid turbulence associated with creation of dusty plasmas in the near earth space environment," *IEEE Trans. Plasma Sci.*, vol. 40, no. 3, pp. 946–953, 2012.

[15] P. A. Bernhardt, "Probing the magnetosphere using chemical releases from the CRRES satellite," *Phys. Fluids B*, vol. 4, no. 7, pp. 2249–2256, Jul. 1992.

[16] H. G. Booker, "A local reduction of F-region ionization due to missile transit," *J. Geophys. Res.*, vol. 66, no. 4, pp. 1073–1079, 1961.

[17] J. E. Jackson, H. A. Whale, and S. J. Bauer, "Local ionospheric disturbance created by a burning rocket," *J. Geophys. Res.*, vol. 67, no. 5, pp. 2059–2061, 1962.

[18] M. Mendillo, G. S. Hawkins, and J. A. Klobuchar, "A sudden vanishing of the ionospheic F region due to the launch of Skylab," *J. Geophys. Res.*, vol. 80, no. 16, pp. 2217–2225, 1975.

[19] M. Mendillo, "Ionospheric Holes: A review of theory and recent experiments," *Adv. Space Res.*, vol. 8, no. 1, pp. 51–62, 1988.

[20] M. Mendillo, J. Baumgardner, D. P. Allen, J. Foster, J. Holt, G. R. A. Ellis, A. Klekociuk, and G. Reber, "Spacelab-2 plasma depletion experiments for ionospheric and radio astronomical studies," *Science*, vol. 238, no. 4831, pp. 1260–1264, Nov. 1987, DOI:10.1126/science.238.4831.1260.

[21] P. A. Bernhardt, B. A. Kashiwa, C. A. Tepley, and S. T. Noble, "Spacelab 2 upper atmospheric modification experiment over Arecibo, 1, neutral gas dynamics," *Astrophys. Lett. Commun.*, vol. 27, no. 3, pp. 169–181, 1988.

[22] P. A. Bernhardt, W. E. Swartz, M. C. Kelley, M. P. Sulzer, and S. T. Noble, "Spacelab 2 upper atmospheric modification experiment over Arecibo, 2, plasma dynamics," *Astrophys. Lett. Commun.*, vol. 27, no. 3, pp. 183–198, 1988.

[23] J. C. Foster, J. M. Holt, and L. J. Lanzerotti, "Mid-latitude ionospheric perturbation associated with the Spacelab-2 plasma depletion experiment at Millstone Hill," *Ann. Geophys.*, vol. 18, no. 1, pp. 111–119, 2000. DOI:10.1007/s00585-000-0111-1.

[24] M. Mendillo, S. M. Smith, A. Coster, P. Erickson, J. Baumgardner, and C. Martinis, "Man-made space weather," *Space Weather*, vol. 6, p. S09 001, Sep. 2008, DOI:10.1029/2008SW000406.

[25] M. Ozeki and K. Heki, "Ionospheric holes made by ballistic missiles from North Korea detected with a Japanese dense GPS array," *J. Geophys. Res.*, vol. 115, p. A09 314, Sep. 2010, DOI:10.1029/2010JA015531.

[26] M. Rapp and F.-J. Lübken, "Polar mesosphere summer echoes (PMSE): Review of observations and current understanding," *Atmos. Chem. Phys.*, vol. 4, no. 11/12, pp. 2601–2633, Dec. 2004, DOI:10.5194/acp-4-2601-2004.

[27] J. M. Burt and I. D. Boyd, "High-altitude plume simulations for a solid propellant rocket," *AIAA J.*, vol. 45, no. 12, pp. 2872–2884, 2007.

[28] B. L. Jones and J. Tharayil, "Development of a third stage motor for the Black Brant X sounding rocket," in *Proc. AIAA Sounding Rocket Conf.*, Oct. 26–28, 1982, pp. 313–321.

[29] P. A. Bernhardt, J. D. Huba, J. A. Fulford, P. A. Forsyth, D. N. Anderson, and S. T. Zalesak, "Analysis of rocket beacon transmissions to reconstruct ionospheric densities," *Radio Sci.*, vol. 28, no. 4, pp. 613–627, 1993.

[30] P. A. Bernhardt, J. B. Baumgardner, A. N. Bhatt, P. E. Erickson, M. F. Larsen, T. R. Pedersen, and C. L. Siefring, "Optical emissions observed during the charged aerosol release experiment (CARE I) in the ionosphere," *IEEE Trans. Plasma Sci.*, vol. 39, no. 11, pp. 2774–2775, Nov. 2011.

[31] P. A. Bernhardt, J. D. Huba, E. Kudeki, R. F. Woodman, L. Condori, and F. Villanueva, "The lifetime of a depression in the plasma density over Jicamarca produced by space shuttle exhaust in the ionosphere," *Radio Sci.*, vol. 36, no. 5, pp. 1209–1220, 2001.

[32] D. N. Anderson and P. A. Bernhardt, "Modeling of an $H_2$ gas release on the equatorial ionosphere," *J. Geophys. Res.*, vol. 83, no. A10, pp. 4777–4790, 1978.

[33] R. A. Greenwald, K. B. Baker, J. R. Dudeney, M. Pinnock, T. B. Jones, E. C. Thomas, J.-P. Villain, J.-C. Cerisier, C. Senior, C. Hanuise, R. D. Hunsucker, G. Sofko, J. Koehler, E. Nielsen, R. Pellinen, A. D. M. Walker, N. Sato, and H. Yamagishi, "DARN/SuperDARN," *Space Science Reviews*, vol. 71, no. 1–4, pp. 761–796, 1995, DOI:10.1007/BF00751350.

[34] O. da Beaujardière, L. Jeong, B. Basu, S. Basu, T. Beach, P. Bernhardt, W. Burke, K. Groves, R. Heelis, R. Holzworth, C. Huang, D. Hunton, M. Kelley, R. Pfaff, J. Retterer, F. Rich, N. Starks, P. Straus, and C. Valladares, "C/NOFS: A mission to forecast scintillations," *J. Atmos. Solar-Terr. Phys.*, vol. 66, no. 17, pp. 1573–1591, Nov. 2004.

[35] B. D. Hester, Y.-H. Chiu, J. R. Winick, R. A. Dressler, L. S. Bernstein, M. Braunstein, and P.-F. Sydney, "Analysis of space shuttle primary reaction-control engine-exhaust transients," *J. Spacecraft Rockets*, vol. 46, no. 3, pp. 679–688, May–Jun. 2009, DOI:10.2514/1.39516.

[36] K. C. Yeh and C. H. Liu, *Theory of Ionospheric Waves*. New York: Academic, 1972.

**P. A. Bernhardt**, photograph and biography not available at the time of publication.

**J. O. Ballenthin**, photograph and biography not available at the time of publication.

**J. L. Baumgardner**, photograph and biography not available at the time of publication.

**A. Bhatt**, photograph and biography not available at the time of publication.

**I. D. Boyd**, photograph and biography not available at the time of publication.

**J. M. Burt**, photograph and biography not available at the time of publication.

**R. G. Caton**, photograph and biography not available at the time of publication.

**A. Coster**, photograph and biography not available at the time of publication.

**P. J. Erickson**, photograph and biography not available at the time of publication.

**J. D. Huba**, photograph and biography not available at the time of publication.

**G. D. Earle**, photograph and biography not available at the time of publication.

**C. R. Kaplan**, photograph and biography not available at the time of publication.

**J. C. Foster**, photograph and biography not available at the time of publication.

**K. M. Groves**, photograph and biography not available at the time of publication.

**R. A. Haaser**, photograph and biography not available at the time of publication.

**R. A. Heelis**, photograph and biography not available at the time of publication.

**D. E. Hunton**, photograph and biography not available at the time of publication.

**D. L. Hysell**, photograph and biography not available at the time of publication.

**J. H. Klenzing**, photograph and biography not available at the time of publication.

**M. F. Larsen**, photograph and biography not available at the time of publication.

**F. D. Lind**, photograph and biography not available at the time of publication.

**T. R. Pedersen**, photograph and biography not available at the time of publication.

**R. F. Pfaff**, photograph and biography not available at the time of publication.

**R. A. Stoneback**, photograph and biography not available at the time of publication.

**P. A. Roddy**, photograph and biography not available at the time of publication.

**S. P. Rodriquez**, photograph and biography not available at the time of publication.

**G. S. San Antonio**, photograph and biography not available at the time of publication.

**P. W. Schuck**, photograph and biography not available at the time of publication.

**C. L. Siefring**, photograph and biography not available at the time of publication.

**C. A. Selcher**, photograph and biography not available at the time of publication.

**S. M. Smith**, photograph and biography not available at the time of publication.

**E. R. Talaat**, photograph and biography not available at the time of publication.

**J. F. Thomason**, photograph and biography not available at the time of publication.

**R. T. Tsunoda**, photograph and biography not available at the time of publication.

**R. H. Varney**, photograph and biography not available at the time of publication.